REPORT DOCUMENTATION PAGE

Form Approved
OMB No. 0704-0188

1. REPORT DATE *(DD-MM-YYYY)*	**2. REPORT TYPE**	**3. DATES COVERED** *(From - To)*
May 2009	Master's Thesis	1 May 2009 – 10 February 2015

4. TITLE AND SUBTITLE
TRANSIENT LIFT OFF TESTING RESULTS FOR A RADIAL HYBRID BEARING

5a. CONTRACT NUMBER
FA9300-04-C-0016

5b. GRANT NUMBER

5c. PROGRAM ELEMENT NUMBER

6. AUTHOR(S)
RALPH HENRY BORCHARD

5d. PROJECT NUMBER

5e. TASK NUMBER

5f. WORK UNIT NUMBER
Q0BY

7. PERFORMING ORGANIZATION NAME(S) AND ADDRESS(ES)

Air Force Research Laboratory (AFMC)
AFRL/RQRC
10 E. Saturn Blvd
Edwards AFB, CA 93524-7680

8. PERFORMING ORGANIZATION REPORT NO.

9. SPONSORING / MONITORING AGENCY NAME(S) AND ADDRESS(ES)

Air Force Research Laboratory (AFMC)
AFRL/RQR
5 Pollux Drive
Edwards AFB, CA 93524-7048

10. SPONSOR/MONITOR'S ACRONYM(S)

11. SPONSOR/MONITOR'S REPORT NUMBER(S)
AFRL-RQ-ED-OT-2015-040

12. DISTRIBUTION / AVAILABILITY STATEMENT
Approved for public release; distribution unlimited

13. SUPPLEMENTARY NOTES
PA Case Number: #15070; Clearance Date: 2/10/2015
This is a Master's Thesis based upon work subcontracted to Texas A&M University by Northrop Grumman under the USET contract. The work was completed in 2008 and the advisor is looking to have the thesis made publicly releasable.

14. ABSTRACT
An experimental test rig was designed and developed to test the performance of a hybrid bearing during its initial lift-off, referred to as start transient. The hybrid bearing studied was designed to replicate the geometry of the bearing used in a new Liquid Hydrogen Turbopump. The test rig uses a high-speed spindle motor capable of 20,000 RPM that drives a 782 Inconel rotor connected by a high speed flexible coupling. The rotor was supported by ceramic ball bearings on the coupling end, and the test hybrid bearing at the other end. A magnetic bearing is utilized to apply loads to the rotor at mid-span. During testing, several factors were varied including ramp rate (rpm/sec) to vary drive torque, supply pressure, applied loading, and load orientation to simulate various start transient scenarios. This data was analyzed in an attempt to quantify hydrodynamic and hydrostatic lift-off speeds. Hydrodynamic lift-off occurs when the rotational speed of the rotor causes the wedge effect of the film to overcome forces acting on the rotor, while hydrostatic lift-off occurs when the pressure (which is speed dependent) developed in the bearing overcomes the forces acting on the rotor to cause lift-off. The lift-off speed is an important quantity to determine for a certain condition to prevent rotor and bearing damage due to a prolonged rotor/bearing contact. With the rotor being loaded with a static force of 1X rotor weight in the vertical direction, it lifted-off hydrostatically at 4275 RPM. In the case of higher static vertical load, 8X rotor weight, it lifted-off hydrostatically at 7900 RPM. Testing showed that an increase in load and ramp rate increases the speed at which the rotor lifted-off. From this outcome, the hydrostatic lift-off is highly dependent on supply pressure and can be determined by graphical means. Although attempts were made to quantify hydrodynamic lift-off, the data showed no reliable indicators. To avoid damage during start transients, the hydrostatic lift-off speed must be minimized, decreasing the time the rotor rubs the surface of the bearing.

15. SUBJECT TERMS
N/A

16. SECURITY CLASSIFICATION OF:			**17. LIMITATION OF ABSTRACT**	**18. NUMBER OF PAGES**	**19a. NAME OF RESPONSIBLE PERSON**
					G. Ruderman
a. REPORT	**b. ABSTRACT**	**c. THIS PAGE**	SAR	55	**19b. TELEPHONE NO** *(include area code)*
Unclassified	**Unclassified**	**Unclassified**			N/A

Standard Form 298 (Rev. 8-98)
Prescribed by ANSI Std. 239.18

TRANSIENT LIFT OFF TESTING RESULTS FOR A RADIAL HYBRID BEARING

A Project Report

By

RALPH HENRY BORCHARD

Submitted
In partial fulfillment of the requirements for the degree of

MASTER OF SCIENCE

May 2009

Major Subject: Mechanical Engineering

Abstract

Transient Testing Results for an Experimental Hybrid Bearing

(May 2009)

Ralph Henry Borchard, B.S.M.E., Texas A&M University

M.S.M.E., Texas A&M University

Chair of Advisory Committee: Dr. Dara Childs

An experimental test rig was designed and developed to test the performance of a hybrid bearing during its initial lift-off, referred to as start transient. The hybrid bearing studied was designed to replicate the geometry of the bearing used in a new Liquid Hydrogen Turbopump. The test rig uses a high-speed spindle motor capable of 20,000 RPM that drives a 782 Inconel rotor connected by a high speed flexible coupling. The rotor was supported by ceramic ball bearings on the coupling end, and the test hybrid bearing at the other end. A magnetic bearing is utilized to apply loads to the rotor at mid-span. During testing, several factors were varied including ramp rate (rpm/sec) to vary drive torque, supply pressure, applied loading, and load orientation to simulate various start transient scenarios. This data was analyzed in an attempt to quantify hydrodynamic and hydrostatic lift-off speeds. Hydrodynamic lift-off occurs when the rotational speed of the rotor causes the wedge effect of the film to overcome forces acting on the rotor, while hydrostatic lift-off occurs when the pressure (which is speed dependent) developed in the bearing overcomes the forces acting on the rotor to cause lift-off. The lift-off speed is an important quantity to determine for a certain condition to prevent rotor and bearing damage due to a prolonged rotor/bearing contact. With the rotor being loaded with a static force of 1X rotor weight in the vertical direction, it lifted-off hydrostatically at 4275 RPM. In the case of higher static vertical load, 8X rotor weight, it lifted-off hydrostatically at 7900 RPM. Testing showed that an increase in load and ramp rate increases the speed at which the rotor lifted-off. From this outcome, the hydrostatic lift-off is highly dependent on supply pressure and can be determined by graphical means. Although attempts were made to quantify hydrodynamic lift-off, the data showed no reliable indicators. To avoid damage during start transients, the hydrostatic lift-off speed must be minimized, decreasing the time the rotor rubs the surface of the bearing.

Acknowledgements

I must first thank Dr. Childs for granting me the opportunity to work and research at the Texas A&M Turbomachinery Laboratory. I cannot put down on paper the many lessons I have learned in life and rotordynamics during my time under his supervision at the lab. Special thanks to Northrop Grumman Space Technology (NGST) for their support for this research project. I also must thank Dr. Ed Marotta and many other colleagues for convincing me to come back to graduate school. Special thanks to my parents who supported me in whatever I wanted to accomplish. Both parents worked hard for me to attend higher education, and I am forever thankful for their generosity. I also like to thank my wonderful wife Krista, whom has been very patient with me throughout this process, and has proved her love of me time and time again. With the above support, achieving a Master of Science in Mechanical Engineering has been accomplished. This goal would not have been accomplished without the help of the previous work done by my peers Dustin Pavelek and B.J. Dyck, and continuous help provided by David Mertz and Stephen Phillips. I am forever in debt to those who sacrificed time and effort for me.

Table of Contents

List of Figures

List of Tables

Introduction

Hydrostatic bearings are increasingly being used in rocket engine turbo-pumps as a viable replacement for ball bearings due to their Diameter X Speed (DN) life. Hydrostatic bearings have some damping and a very high load capacity due to an external pressurized supply and a flow restrictor. One of the benefits of the hydrostatic bearing for a turbo-pump and cryogenic applications is that the direct stiffness and load capacity are largely independent of the lubricant viscosity. This proves useful when the lubricant is a process fluid like liquid oxygen or liquid hydrogen.

Previous efforts by Pratt and Whitney under supervision from United States Air Force Research Laboratory (AFRL), during their recent design of the new Advanced Liquid Hydrogen (ALH) Turbo-pump, utilized hydrostatic bearings. During testing of the design, several attempts to reach design speed failed. Initial suspicions of the failed test were believed to be due to dry-friction whirl, which is characterized by rotor-stator contact. During this contact, the rotor rolls without slipping along the bearing surface creating a large drag-torque on the rotor. This large drag torque could have limited the maximum speed that the rotor was able to obtain during testing. Since the supply pressure of the liquid hydrogen to the bearing is a function of the rotor speed squared, the bearing never reached full operating pressure. The root cause of the failed program was not known at the time and led to a new effort to develop better design tools for predicting the transient behavior of the turbo-pump during start-up.

To create these new design tools, a test program was needed to validate the theoretical predictions from computer codes. The following discussion will explain the hybrid bearing test program and present the results from the transient testing.

Transient Hybrid Bearing Previous Work

Several papers have been published on steady-state performance of hydrostatic bearings and test data [1]. Childs and Hale show good agreement between test results and predictions for rotordynamic coefficients up to a 0.5 eccentricity ratio. But, there is a lack of published data on transient hydrostatic bearing performance.

Scharrer et al. designed a test rig based on start transients of the Space Shuttle Main Engine (SSME) High Pressure Oxidizer Turbo-pump (HPOTP) and conducted start transients for hydrostatic bearings in liquid nitrogen [2]. To design the test rig, care was taken to match pressure and loading profiles of the SSME HPOTP. A servo-valve control scheme was implemented to control the supply pressure to the bearing that varied with speed squared. Load was varied both linearly with speed and speed squared. These experiments tested a hydrostatic journal bearing in liquid nitrogen with scalloped recesses [3]. Several different bearings underwent testing, but the most common geometry is in Table 1.

Table 1. Bearing geometry from Scharrer et al. [3]

Bearing Length	31.75 mm (1.25 in)
Bearing Diameter	76.2 mm (3.0 in)
Operating Radial Clearance	0.084 mm (0.0033 in)
Number of Recesses	6
Recess Area Ratio	0.12
Recess Axial Length	11.1 mm (0.438 in)
Recess Circ. Length	13.3 mm (0.524 in)
Recess Depth	0.254 mm (0.01 in)
Orifice Diameter	1.3 mm (0.051 in)

For these tests, Scharrer et al. [3] stated that the reversal in shaft direction from clockwise to counter-clockwise indicates the inception of hydrodynamic lift-off, as demonstrated in Fig. 1.

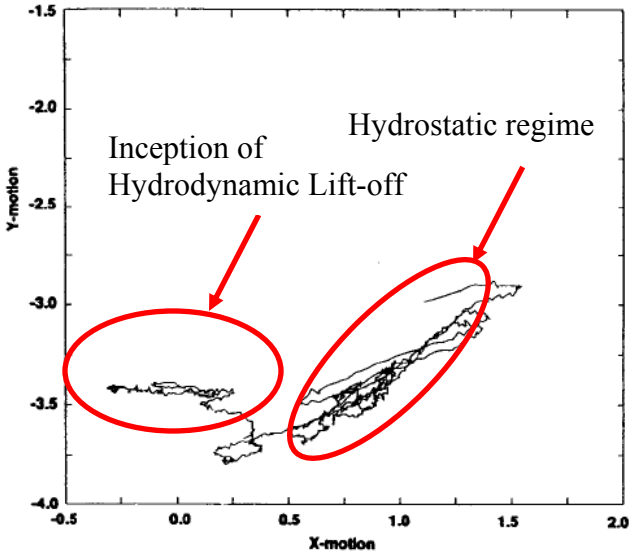

Fig. 1. Hydrodynamic lift-off and hydrostatic regime from Scharrer et al. [3].

At the end of the testing, Scharrer et al.[3] concluded that the combination of hard journal materials (Chrome-Plated NiCr and PS212-Coated NiCr) and soft bearing materials (Carbon P5N, Ag-Plated NiCr, and Nickel Chromium Alloy) resulted in immeasurable wear for the hydrostatic bearing after 337 tests. They also concluded that the hydrostatic bearing can withstand the loads of the same magnitude as turbo-pumps. No quantifiable determination of lift-off was made due to a design that supplied pressure before start-up.

Scharrer et al. [4] later performed tests using liquid oxygen with a bearing diameter of 3.36 in (85.3 mm) and a bearing length of 1.25 in (31.75 mm). This particular tapered journal bearing (Lomakin) had C_b/R_b = 0.00655 at the entrance and C_b/R_b = 0.00155 at the exit. Equation 1 gives the definition of C_b/R_b.

$$\frac{C_b}{R_b} = \frac{Diametral\ Clearance}{Bearing\ Radius} \tag{1}$$

The Lomakin bearing uses a tapered diametral clearance axially that creates a velocity difference in the lubricating medium. This velocity difference creates an increased stiffness effect due to the lubricating medium. Hydrodynamic and hydrostatic lift-off were determined using proximity probes and by observing changes in the speed profile. The results are in Fig. 2.

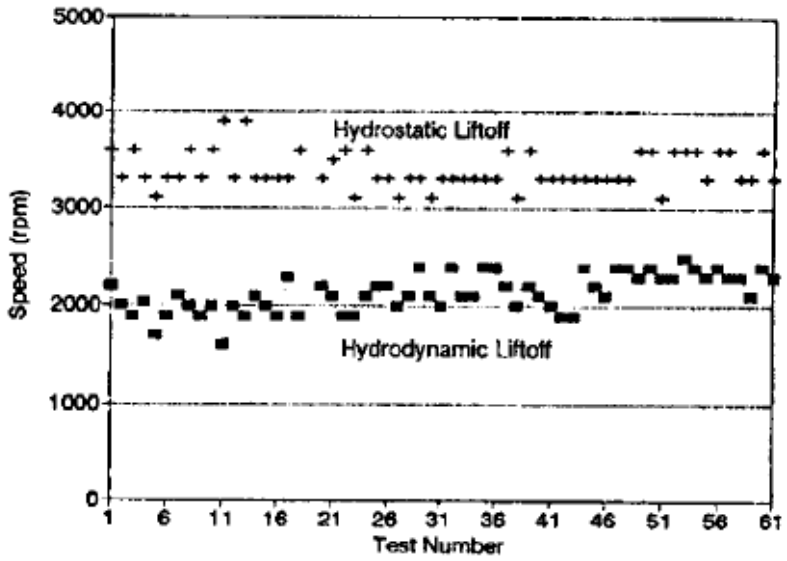

Fig. 2. Lift-off testing from Scharrer et al. [4].

Typical shaft centerline results from Scharrer et al. [4] are seen in Fig. 3. This figure illustrates little difference between the first and last test exists in the centerline, and the rotor seems to center itself in the bearing even after sixty start transients.

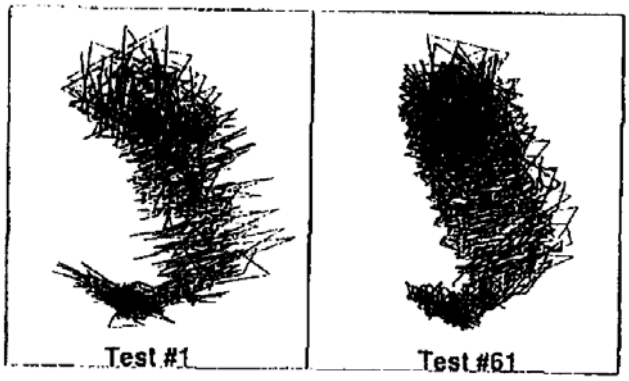

Fig. 3. Complete shaft centerline plots from Scharrer et al.[4].

After testing was complete, a close inspection of the wear was completed. Wear was evident in an 80˚ arc in the direction of load with both burnishing of the bearing surface and debris formation. Figure 4 depicts the wear associated with the bearing from the start transients.

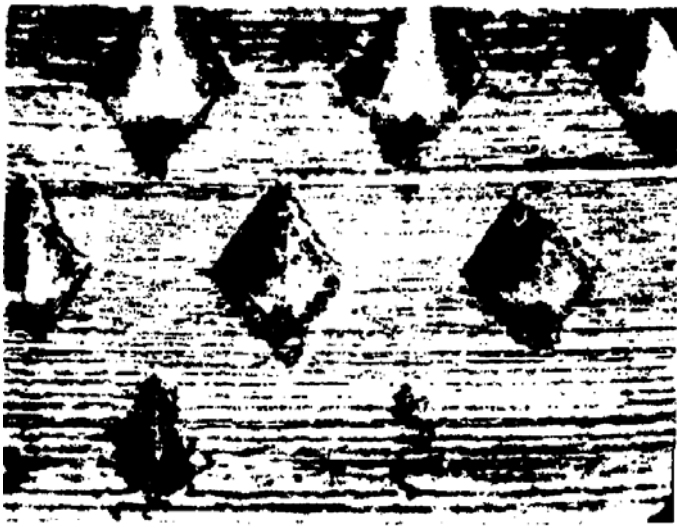

Fig. 4. Burnishing of the bearing surface after sixty start transients [4].

Even though the work by Scharrer et al. [4] proves to be a good indicator of the start transient behavior (bearing wear and shaft centerlines) for hydrostatic bearings, it mainly focuses on the influence of bearing-rotor material combinations and a Lomakin bearing. Their published data proves to be inadequate to calibrate a computer code for predicting transient bearing performance. Scharrer et al. produced results for a Lomakin bearing, NGST is proposing to use a real hydrostatic radial bearing in the redesign of the turbopump, and the following will discuss the performance testing and results of a hydrostatic bearing.

Test Rig and Hardware Description

Initial research and design of the test facilities and hardware were performed by both Pavelek [5] and Dyck [6]. Thorough design analysis for specific test rig hardware was performed by Pavelek [5], and the initial assembly drawing of the test rig set-up can be viewed in Fig. 5.

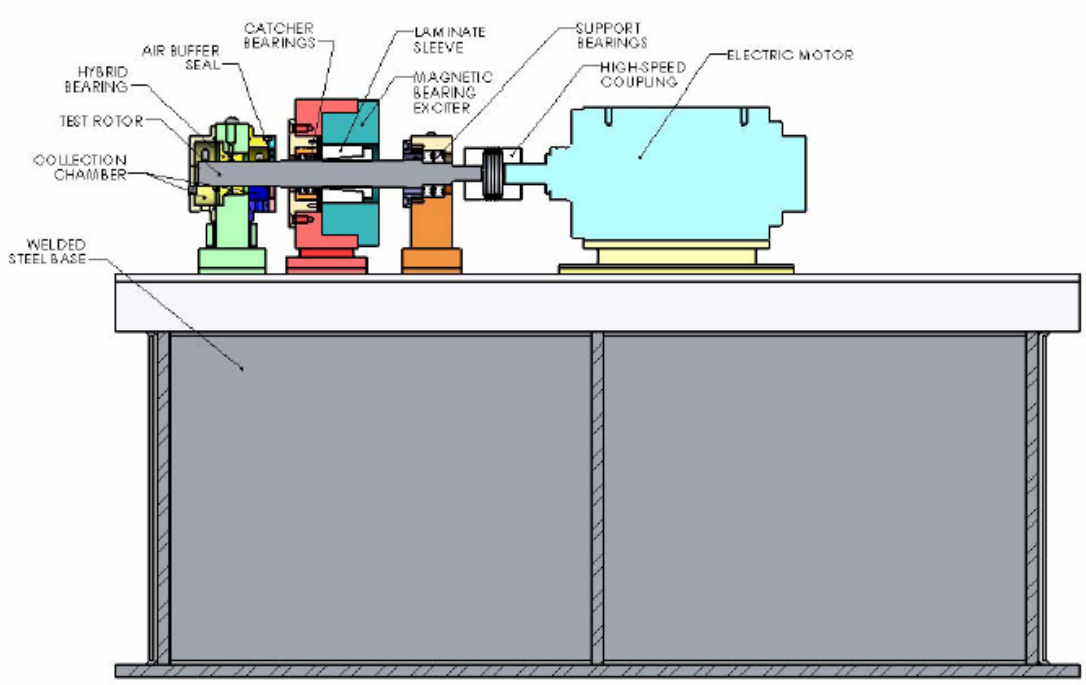

Fig. 5. Cross-sectional view of the designed transient radial bearing test rig by Pavelek [5].

Major test components for the test set up consisted of the hybrid bearing, magnetic bearing exciter, and test rotor.

Test Bearing

The test bearing design is consistent with the proposed turbo-pump bearing in terms of clearance, diameter, and number of recesses. The designed bearing is illustrated in Fig. 6.

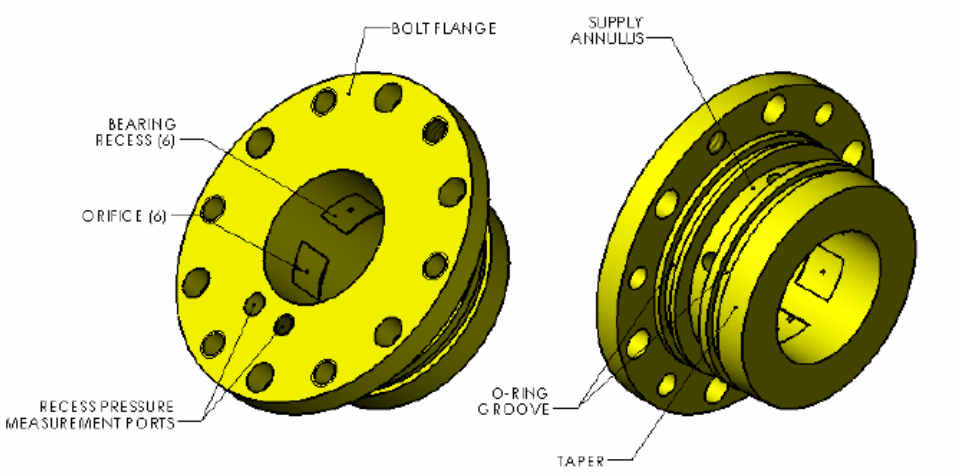

Fig. 6. Hybrid bearing design from Solidworks by Pavelek [6].

The bearing features two recess pressure measurement ports that were utilized in the performance testing. Ports are provided for the measurement of both static and dynamic pressure within the recess of the bearing. The bearing itself was securely mounted to a bearing housing which allowed for further instrumentation mounting for performance evaluation, as well as the ports for supplied water entrance to the bearing supply annulus. Fig. 7 depicts a cross-section of the housing assembly.

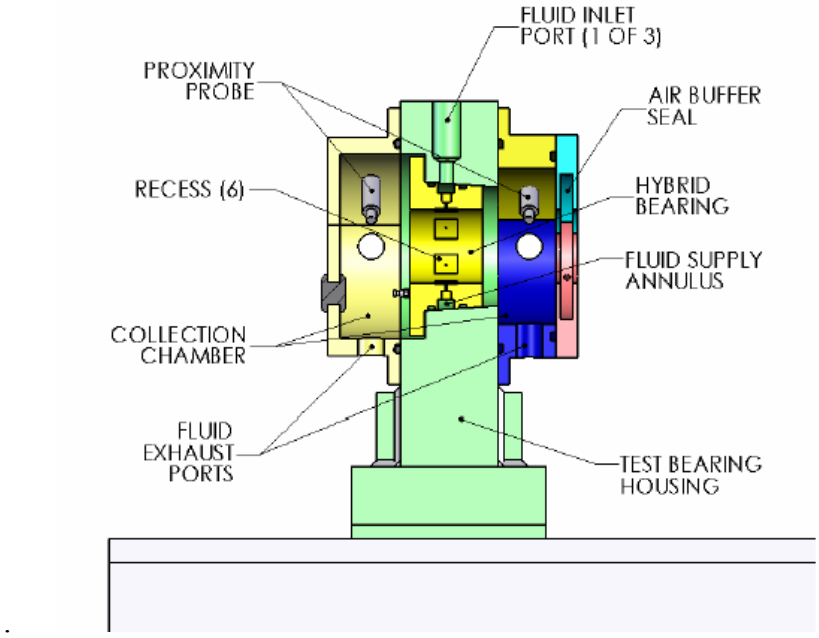

Fig. 7. Cross-sectional view from Solidworks of the test bearing support pedestal by Pavelek [5].

After the water has passed through the bearing, it is collected and exhausted to an external sump tank to be re-circulated back to the supply. The computer code

HYDROJET© was utilized in the design of the test bearing by Pavelek [5]. A summary of the design parameters are in Table 2.

Table 2. Summary of the design parameters for the Hybrid bearing [5].

Bearing Geometric Parameters		
Parameter	Value	Units
Diameter	3.81E-02	[m]
Axial Length	3.81E-02	[m]
Inlet Radial Clearance	6.35E-05	[m]
Exit Radial Clearance	6.35E-05	[m]
# Pockets	6	[-]
Pocket_axial_length	1.20E-02	[m]
Pocket 1 - leading edge	24	[deg]
Pocket 1 - arc length	36	[deg]
Pocket depth	5.08E-04	[m]
Orifice diameter	1.19E-03	[m]
Orifice discharge coefficient	0.85	[-]
Orifice angle injection	0	[-]
Orifice location relative to pocket	0.5	[-]
Pocket Area Ratio	0.1875	[-]

Supply Fluid Properties (Water)		
Parameter	Value	Units
Supply Temperature	54	[C]
Cavitation Pressure	0.006895	[bar]
Viscosity at TS, PS	5.01E-04	[Ns/m^2]
Density at TS, PS	984.33	[kg/m^3]
Viscosity at TS, PA	5.01E-04	[Ns/m^2]
Density at TS, PA	983.5	[kg/m^3]
Compressibility	4.64E-10	[m^2/N]

Test results from Mosher and Childs [7] demonstrated that an optimum pressure ratio (recess pressure divided by supply pressure) exists for hybrid bearings between 0.45-0.50 for steady-state applications. An orifice diameter of 1.19 mm (0.047 in) was selected because a pressure ratio of 0.50 is predicted at a speed of 15,000 RPM with a supply pressure of 18.3 bar (265 psia).

Figure 8 shows the design components assembled together on the test stand. Special care was taken during component installation to minimize misalignment and rust formation. Machined surfaces were coated with a mist oil to prevent rust from forming. Laser alignment was utilized to align the rotor to the motor at the coupling.

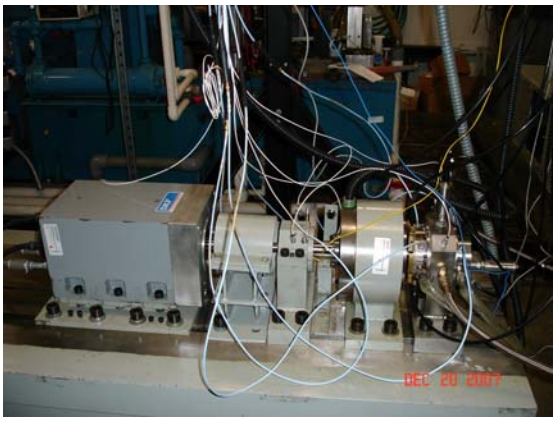

Fig. 8. Assembly of the test bearing and components.

Figure 9 is a close up view of the test bearing pedestal showing all the instrumentation involved in testing.

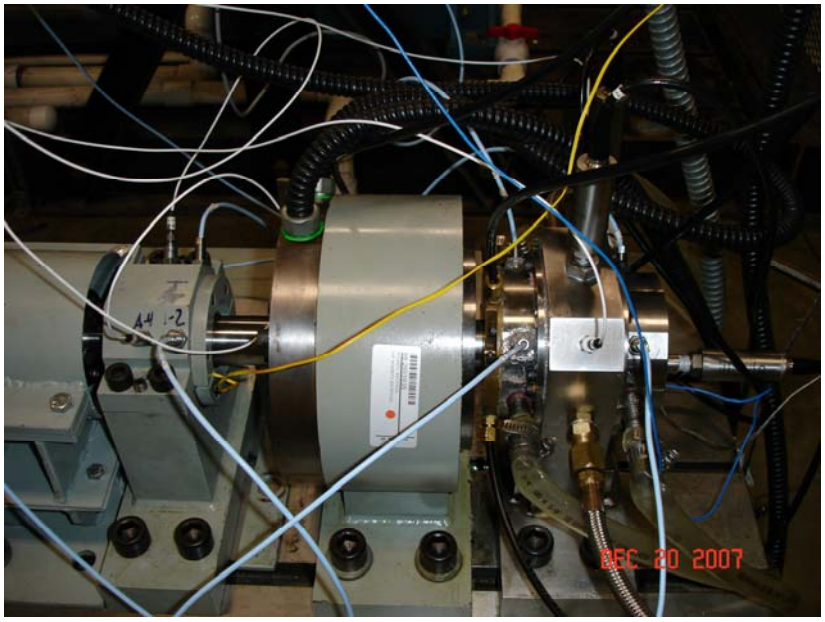

Fig. 9. Close up view of the test bearing support pedestal and instrumentation.

Output from the following list of instrumentation was recorded during testing on a .dat file in LabView:

1. Proximity probes (6 probes at 3 radial locations)
2. Accelerometers (5 sensors at 3 radial locations)
3. Pressure Transducers (3 probes at 3 locations including supply, recess at bottom pocket, and exhaust pressures)
4. Dynamic Pressure Transducer
5. Speed (1 from optical tachometer)
6. Temperature (2 Resistance Temperature Displays for supply and exhaust temperatures)
7. Flow meter (1 flow meter)

Table 3 gives the specification details for each of the instrumentation hardware.

Table 3. Instrumentation specifications detailed for the sensors.

	Location	Manufacturer	Model	Sensitivity	Measurement Range	Frequency Range
	Proximity Probes					
1	Support Bearing Housing	Bently Nevada	3300 REBAM ®	78.7 mV/mm (200mV/mil)	0-0.2 mm (0 - 8mil) (± 6.4 µm, ± 0.25 mil)	0-10,000 Hz +5%,-10%
	(2 probes mounted at 90 deg)					
2	Test Bearing Housing (Inboard)	Bently Nevada	3300 REBAM ®	78.7 mV/mm (200mV/mil)	0-0.2 mm (0 - 8mil) (± 6.4 µm, ± 0.25 mil)	0-10,000 Hz +5%,-10%
	(2 probes mounted at 90 deg)					
3	Test Bearing Housing (Outboard)	Bently Nevada	3300 REBAM ®	78.7 mV/mm (200mV/mil)	0-0.2 mm (0 - 8mil) (± 6.4 µm, ± 0.25 mil)	0-10,000 Hz +5%,-10%
	(2 probes mounted at 90 deg)					
	Accelerometers					
1	Support Bearing Housing	PCB Piezotronics	352C34	100 mV/g (± 10%)	± 50 g pk	0.5 - 10,000 Hz (± 5%)
	(2 probes mounted at 90 deg)					0.3 - 15,000 Hz (± 10%)
2	Test Bearing Housing	PCB Piezotronics	352C34	100 mV/g (± 10%)	± 50 g pk	0.5 - 10,000 Hz (± 5%)
	(2 probes mounted at 90 deg)					0.3 - 15,000 Hz (± 10%)
3	Drive Motor Casing	PCB Piezotronics	393A03	1000 mV/g (± 5%)	± 5 g pk	0.5 - 2000 Hz (± 5%)
	(1 probe mounted by Inboard Bearing)					0.3 - 4000 Hz (± 10%)
	Pressure Transducers					
1	Supply Pressure	PCB Piezotronics	1501B01FB - 1000 psig/20	72.5 mV/bar (5mV/psi) (± 2 %)	0-68.9 bar (0-1000 psig) (± 0.25%)	5-2000 Hz
	(Mounted before test bearing)					
2	Recess Pressure	PCB Piezotronics	1501B01FB - 1000 psig/20	72.5 mV/bar (5mV/psi) (± 2 %)	0-68.9 bar (0-1000 psig) (± 0.25%)	5-2000 Hz
	(Mounted in recess of test bearing)					
3	Exhaust Pressure	PCB Piezotronics	1501B01FB - 1000 psig/20	72.5 mV/bar (5mV/psi) (± 2 %)	0-68.9 bar (0-1000 psig) (± 0.25%)	5-2000 Hz
	(Mounted after test bearing)					
4	Dynamic Pressure	PCB Piezotronics	105C12	72.5 mV/bar (5mV/psi) (± 15 %)	0-68.9 bar (0-1000 psig)	0.5 - 250,000 Hz
	(Mounted in recess of test bearing)					
	Speed					
1	Mounted Tachometer	NIDEC-SHIMPO	MCS - 655	Once per Rev Pulse (Black/White)	N/A	N/A
	Temperature					
1	Supply Temperature	Omega	RTD-NPT-360-E	0.00385 Ω/Ω/ºC	(0- 230ºC) 0-450ºF	N/A
	(Mounted before test bearing)					
2	Exhaust Temperature	Omega	RTD-NPT-360-E	0.00385 Ω/Ω/ºC	(0- 230ºC) 0-450ºF	N/A
	(Mounted after test bearing)					
	Flow					
1	Flow meter	Flow Technology	FT-08AEXW-LEG-5	N/A	0.066 - 2.64 Liters/min (0.25 - 10 gpm)	N/A
	(Mounted before test bearing)					

Other readings that were recorded via the motor controller software included load and an encoder signal for speed. Both Pavelek [5] and Dyck [6] have included specific details in regards to the instrumentation. All instrumentation data were gathered at 5000 Hz to decrease data saturation. A higher frequency sampling rate was not needed to indicate dry friction whip/whirl due to the conclusion of Dyck [6] who found that whip/whirl was only present when a pristinely and dry clean surface existed. During testing, the surface was wet due to ambient conditions and supply lubricant (water).

Magnetic Bearing Exciter

The magnetic bearing exciter was design by SKF and was used as both a static and dynamic loading mechanism. Fig. 10 shows a cross-sectional view of the magnetic bearing.

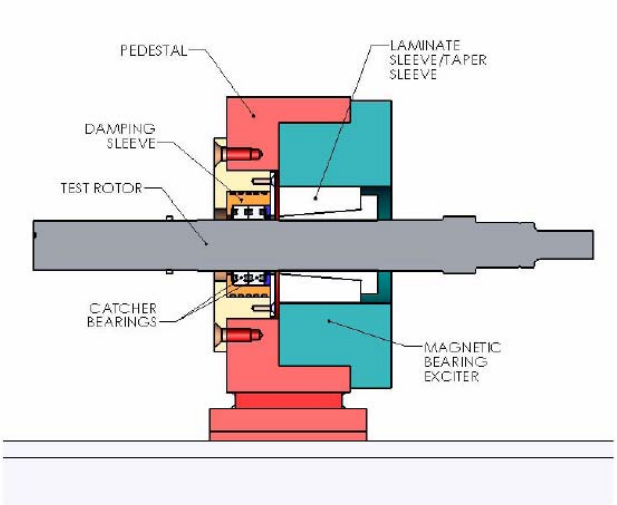

Fig. 10. Cross-sectional view from Solidworks of the magnetic bearing support pedestal [5].

A laminated sleeve attached to the rotor transmits the magnetic force from the exciter to the rotor. Catcher bearings are designed in the system to prevent damage to the exciter in the case of a loss of power. A controller from SKF converts a voltage signal (0-10 V) to current which determines the amount of load the magnetic bearing applies to the rotor. The load applied is representative of the forces applied to the rotor at start-up, including forces from both the turbo-pump and turbine. The current is sent to an axis channel on the bearing. The axis channels are named V24 (horizontal plane) and W24 (vertical plane) and are 180 degrees apart (referred to as I_{top} and I_{bottom}). The planes are oriented in the vertical and horizontal directions during installation, and a force in these directions is produced by sending current to each specific plane. Equation (2) is used to calculate the amount of force applied with the magnetic bearing.

$$F = C\left[\left(\frac{I_{top}}{2(g-x)}\right)^2 - \left(\frac{I_{bottom}}{2(g-x)}\right)^2\right](10^6) - F_o \qquad (2)$$

Where,

C = Calibration Factor $\left(\frac{N \cdot \mu m^2}{A^2}\right)$

g = Effective Gap (μm)

x = Offset (μm)

F_o = Tare (N)

The calibration factor and effective gap are constants for both axes (C = 11.341 and G = 535.01). The offset is assumed to be zero, while the tare is different for both axes (F_o W24 = -0.064 and F_o V24 = 0.174). The tare is calculated with the rotor centered in the bearing at designed max supply pressure and without any load applied. The "Calibrations Settings" tab in MBScope calculates the tare during this process.

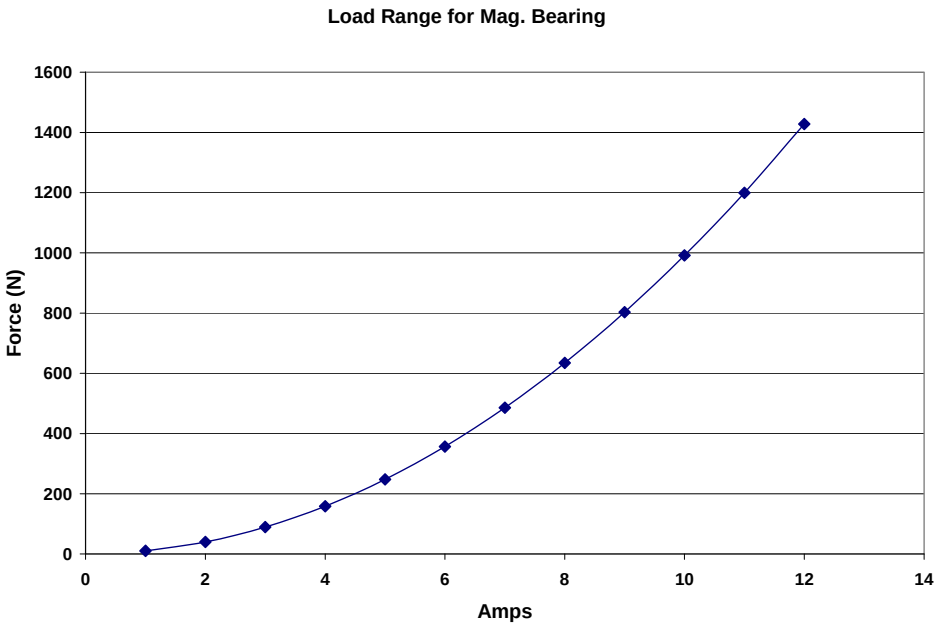

Fig. 11. Graph illustrating the amount of load that the magnetic bearing can apply to the rotor.

Fig. 11 shows the amount of force that was possible for the range of amps. The max load possible is 1423.43 N (320 lbs.) with a 12 Amp current. Using statics, this max force was calculated to be about 840.6 N (191 lbs.) at the bearing. The loading was controlled by the SKF software Sisotune in MBScope. Sisotune specifically controlled the current during the static testing. The actual force was not measured; this was a calculated force based on amps and the magnetic bearing designed force equation from SKF.

Test Rotor

The test rotor was made of 718 Inconel steel, with a bearing span of 308.6 mm (12.149 in.) between a set of ceramic support ball bearings and the test bearing. The diameter of the rotor at the test bearing is 38.1 mm (1.50 in.). A steady-state rotordynamics analysis was conducted by Pavelek [5] using XLTRC^2 Rotordynamics Software. A 32 station model was used in the study and can be seen in Fig. 12.

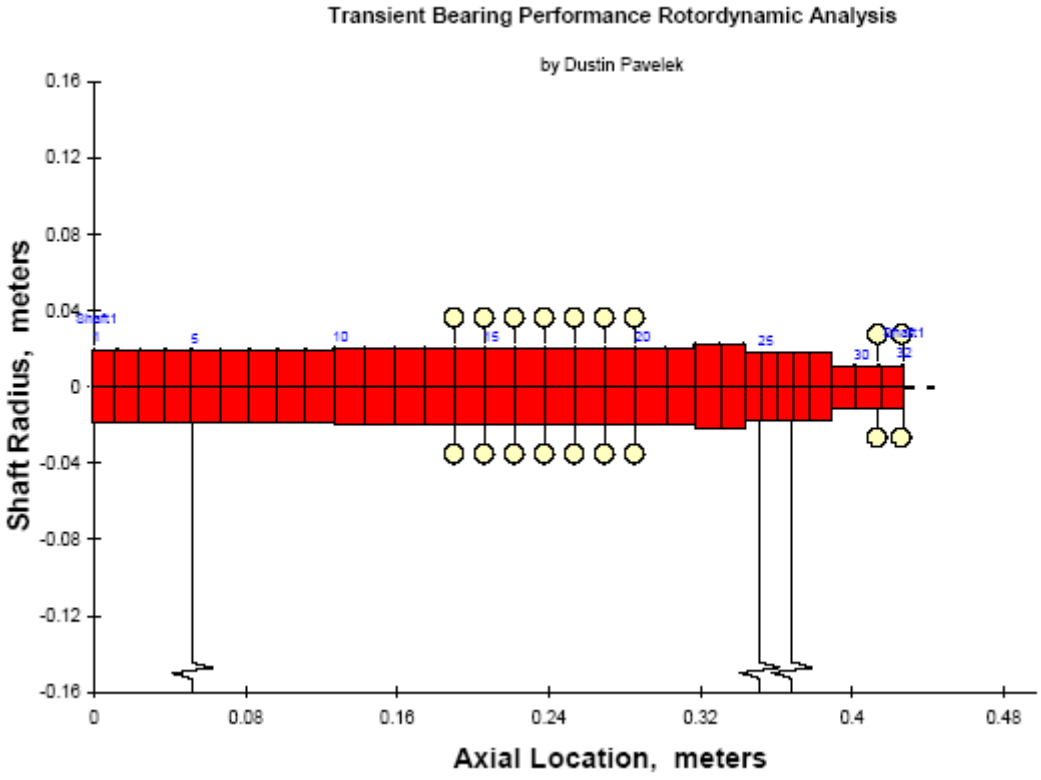

Fig. 12. A 32 station Timoshenko beam model used for the rotordynamic analysis [5].

The model takes into account the stiffness of the support ball bearings, stiffness and damping of the test bearing predicted by HYDROJECT©, and the added mass of the laminated sleeve for the magnetic bearing excitation. Fig. 13 illustrates the results from the rotordynamic analysis created by Pavelek [5].

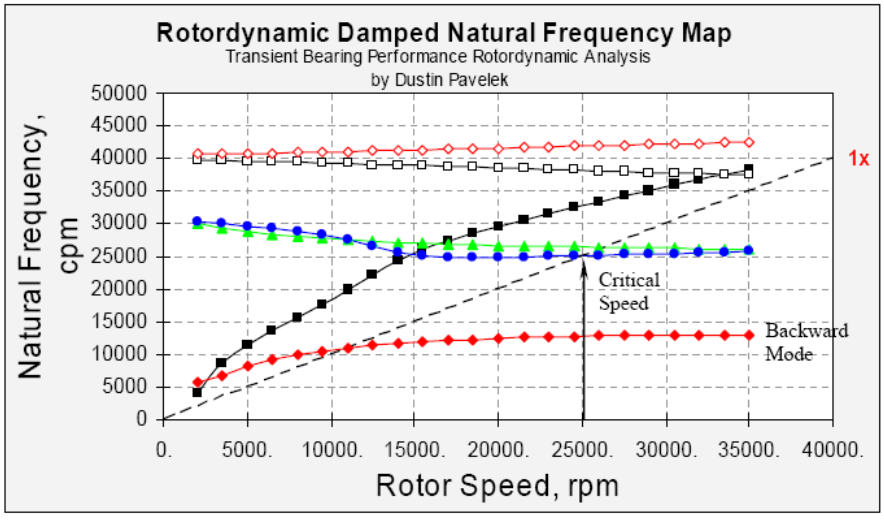

Fig. 13. Rotordynamic damped natural frequency map depicting the first forward critical speed [5].

As seen in the figure, the predicted first backward critical exists at around 11,000 rpm, but is largely damped. The predicted first forward critical is around 25,000 rpm, well above the operating range of the test rig.

Control Valve

A high performance control valve, capable of going fully closed to fully open in less than one second, was needed. The Flowserve air actuated valve also has a built in accumulator that helps maintain stability for valve position in case of severe pressure fluctuations. Fig. 14 illustrates the valve installation as well as its proximity to the test stand.

Fig. 14. Installed control valve.

The valve position was controlled with a 0-10V voltage signal which would be converted to a 1.22-2.05 bar (17.7-29.7 psia) air signal in the valve to open and close depending on the voltage signal. This signal was recorded and outputted using LabView.

Test Rig Testing Design Considerations

Care was taken to match the NGST Radial Test Rig load and speed predictions from the ROCETS code output provided by Northrup Grumman Space Technology. Fig. 15 gives the speed and pressure start transient that needed to be targeted. Parameters of importance were the final supply pressure at 15,000 rpm, which was 8.87 bar (128.7

psia), and time to reach 15,000 rpm. This pressure is the second stage discharge pressure of the pump which varies to the square of speed of the rotor.

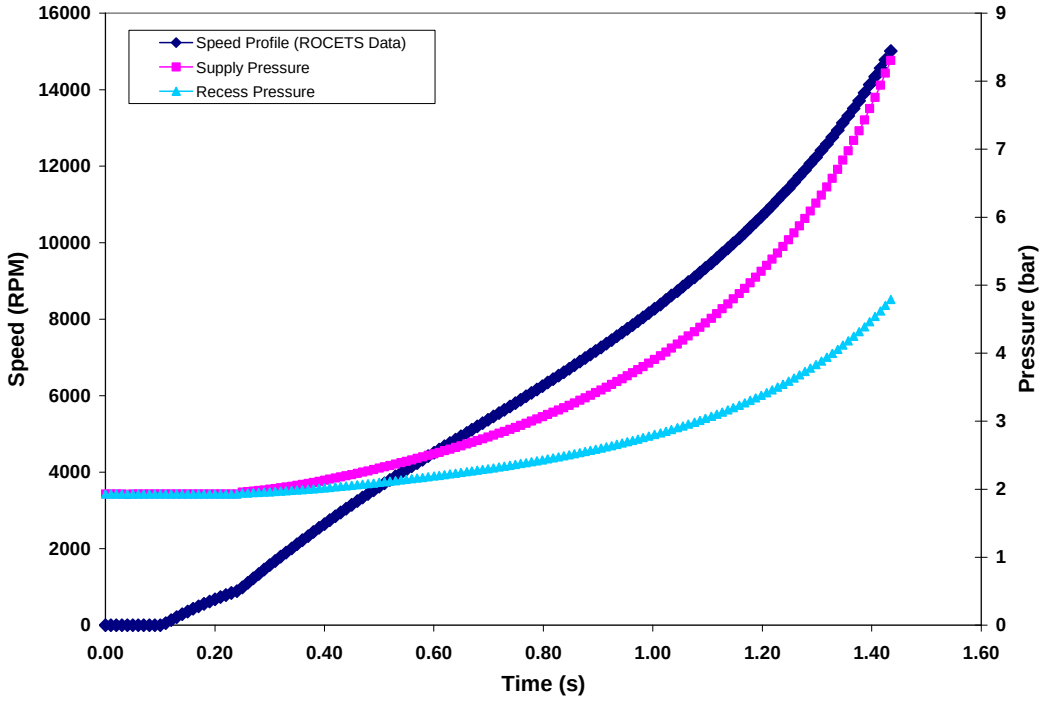

Fig. 15. Speed and pressure versus time from ROCETS provided by NGST for replication.

During initial shakedown testing, it was decided to aim for a supply pressure of 18.3 bar (264.7 psia), doubling the initial supply pressure parameter. The ramp rate corresponding to the ROCETS predictions was found to be 8824 rpm/sec, which corresponds to going 0 to 15,000 rpm in 1.7 sec, for the SKF motor. The best approach to replicate the ROCETS speed profile predictions can be seen in Fig. 16.

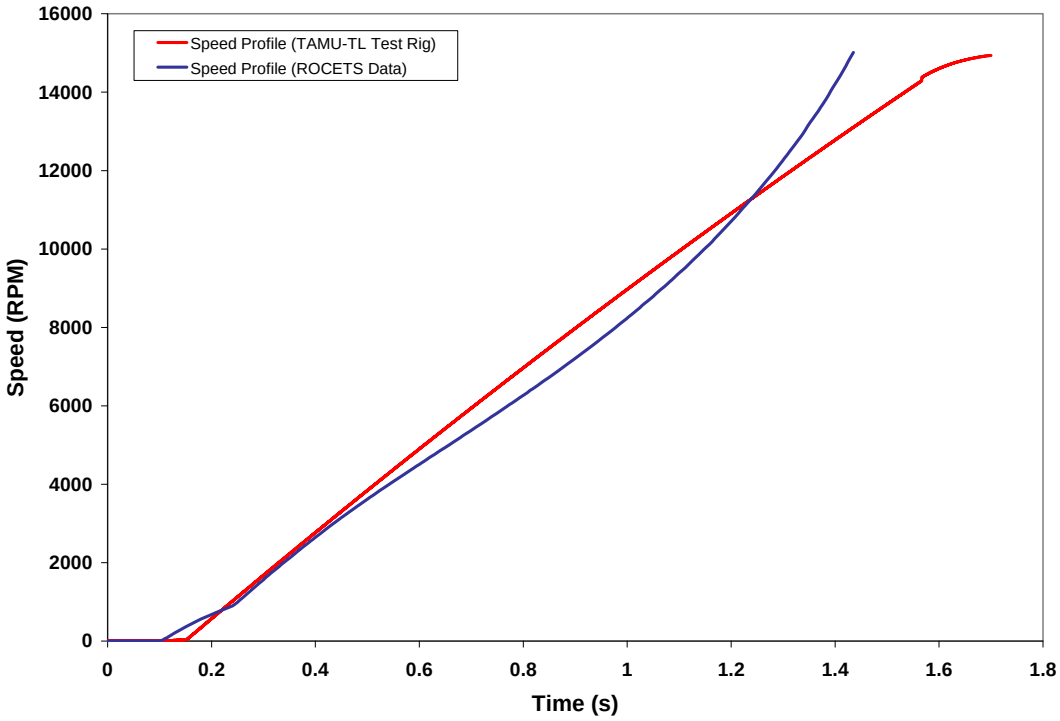

Fig. 16. Comparison of speed versus time between ROCETS and TAMU-TL testing.

The supply pressure was controlled by the control valve position since the total amount of water pressure available was 70 bar (1014.7 psia) and 18.3 bar (264.7 psia) was the set point which was double the original data from ROCETS. Fig. 17 illustrates this difference in set points between ROCETS and the TAMU-TL test rig.

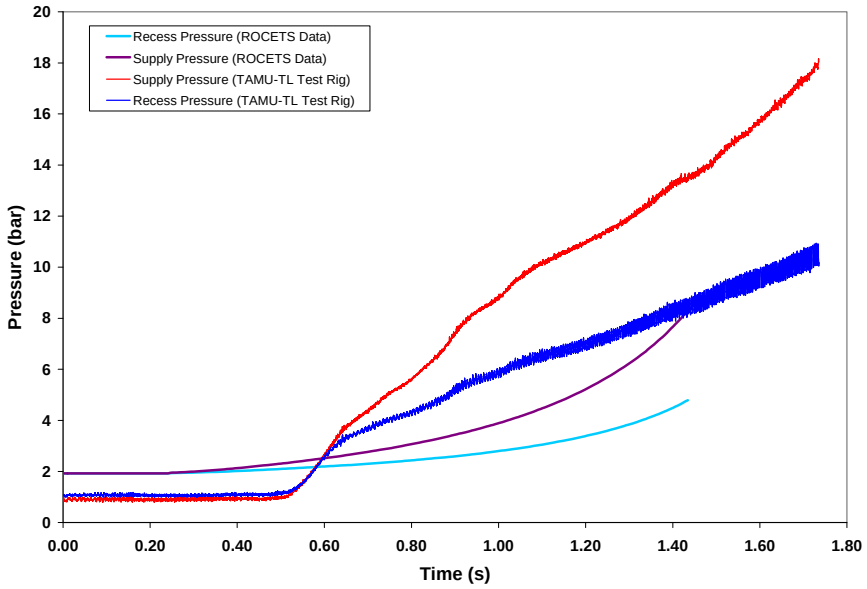

Fig. 17. Comparison of pressure versus time between ROCETS and TAMU-TL testing.

The voltage corresponding to the valve position was varied linearly with speed, which had its own 0-10V voltage signal. This voltage control of pressure was carried out in LabView programming using the custom program Transient.VI. A time delay was also utilized to delay the motor from starting until the water reached the bearing from the valve. This action was needed to account for several feet of pipe between the valve and supply ports to the test bearing pedestal. Figure 16 represents the 100% torque and 100% pressure cases, which will be described later.

Misalignment Issues

The inner diameter of the test bearing was 38.22 mm (1.5048 in.), while the diameter of the rotor was 38.1 mm (1.5 in.). This yielded a measured diameteral clearance of 0.122 mm (0.0048 in.), within 0.0051 mm (0.0002 in.) of the designed clearance, 0.127 mm (0.005 in.). The test bearing was designed to have a matching machined taper on the outside diameter with the inside diameter of the test bearing support pedestal. Several finely threaded stainless steel socket head cap screws (SHCS) fastened the bearing through a bolt flange to the test bearing pedestal. Coarsely threaded stainless steel SHCS were used to lock the test bearing in place axially. When the bearing was secure, bump tests revealed a 0.0508 mm (0.002 in.) clearance (less than half of the design clearance). Feeler gauges were used to confirm the result, but a four-mil thick gauge was able to fit in the clearance gap. This result indicated a cocked or misaligned bearing in the test pedestal. After several attempts to achieve the designed clearance in the bearing from bump tests, troubleshooting the cause of the misalignment took place. The machined taper on the outside diameter of the bearing was found not to agree with specification and to be the cause of the misalignment. To save time, a procedure to align the test bearing with minimal misalignment was developed. The test bearing would be tightened to a certain point to the test pedestal with a four-mil shim in the clearance at the 12:00 position at the rotor. A bump test was performed in both horizontal and vertical directions to confirm the clearance, and then the bearing was secured or adjusted. Once the test bearing was locked with the coarse SHCS, a final resulting clearance was determined from the bump test. If the final clearance was not

within 0.0127 mm (0.0005 in.) of the design clearance, the bearing had to be readjusted. Table 4 shows the result from the above alignment procedure.

Table 4. Clearance results from the bump tests after test bearing installation.

Diametral Clearance Results from Bump Tests

Inboard			Outboard		
Horizontal	124.7 µm	4.91 mils	Horizontal	108.0 µm	4.25 mils
Vertical	122.7 µm	4.83 mils	Vertical	105.2 µm	4.14 mils
RMS	116.3 µm	4.58 mils	RMS	113.8 µm	4.48 mils

Inboard - Side of bearing closest to motor
Outboard - Side of bearing furthest from motor
RMS - Root mean squared result (sqrt(x^2 + y^2))

Even though the results from the bump test showed an almost elliptical clearance, Fig. 18 shows the graphical representation from the 8-point bump test using the magnetic bearing.

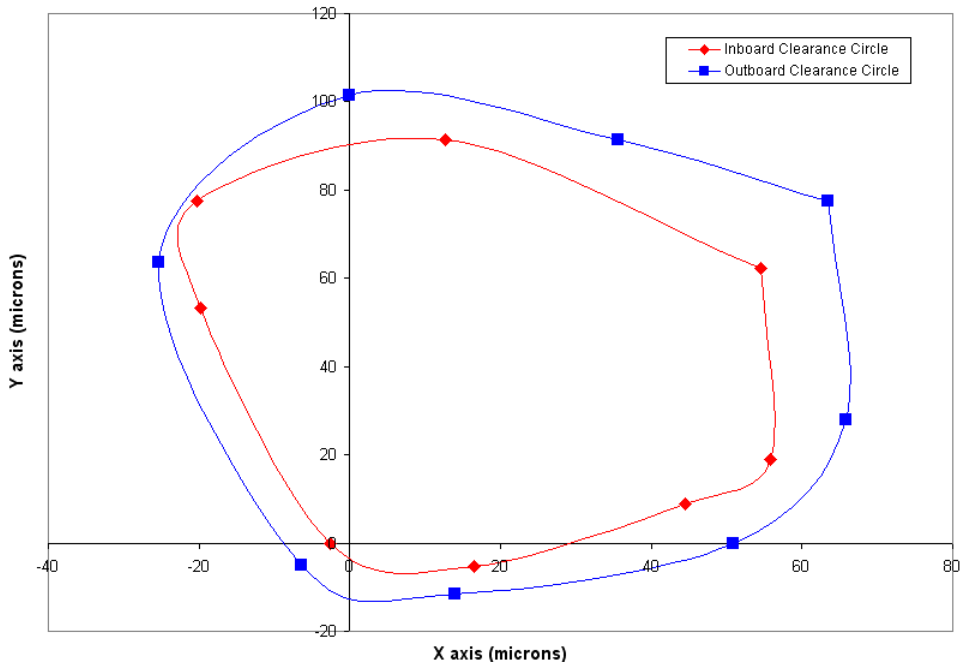

Fig. 18. Clearance circle representation from an 8- point bump test.

This figure shows that the clearance is still not exactly circular. Another issue from this result is that the outboard clearance circle appears slightly smaller than the inboard clearance circle. From this result, it was determined that the loading from the magnetic bearing causes a small rotor bow since Inconel 718 is a soft, ductile metal. The rotor hits

the inboard side of the bearing causing the outboard side to move down almost an average of 0.00635 mm (0.00025 in.) around the entire bearing. Careful attention must be taken when installing the test bearing; any small misalignment will cause an increased pressure ratio and premature rubbing of the rotor onto the bearing.

Test Results

To verify various code parameters, many tests were performed varying ramp rate (to simulate torque ranges), pressure, type of loading, amount of loading, and load orientation. Table 5 summarizes the tests types and classifies them in to cases.

Table 5. NGST Radial Test Rig test matrix.

	Ramp Rate (RPM/sec)	Pressure @ 15,000 rpm	Type of Loading	Load Cases (Multiples of Rotor Weight)	Load Orientation
Case 1	8824	18.3 bar (264.7 psia)	Static	1X, 2X, 3X, 4X, 5X, 6X, 7X, 8X	Load on Pad (Vertical)
Case 2	4412	18.3 bar (264.7 psia)	Static	1X, 2X, 3X, 4X, 5X, 6X, 7X, 8X	Load on Pad (Vertical)
Case 3	4412	9.63 bar (139.7 psia)	Static	1X, 2X, 3X, 4X, 5X, 6X, 7X, 8X	Load on Pad (Vertical)
Case 4	2206	9.63 bar (139.7 psia)	Static	1X, 2X, 3X, 4X, 5X, 6X, 7X, 8X	Load on Pad (Vertical)
Case 5	2206	5.32 bar (77.2 psia)	Static	1X, 2X, 3X, 4X, 5X, 6X, 7X, 8X	Load on Pad (Vertical)
Case 6	8824	18.3 bar (264.7 psia)	Static	1X, 2X, 3X, 4X, 5X, 6X, 7X, 8X	Load on Land (Horizontal)
Case 7	4412	18.3 bar (264.7 psia)	Static	1X, 2X, 3X, 4X, 5X, 6X, 7X, 8X	Load on Land (Horizontal)
Case 8	4412	9.63 bar (139.7 psia)	Static	1X, 2X, 3X, 4X, 5X, 6X, 7X, 8X	Load on Land (Horizontal)
Case 9	2206	9.63 bar (139.7 psia)	Static	1X, 2X, 3X, 4X, 5X, 6X, 7X, 8X	Load on Land (Horizontal)
Case 10	2206	5.32 bar (77.2 psia)	Static	1X, 2X, 3X, 4X, 5X, 6X, 7X, 8X	Load on Land (Horizontal)

Defintions

Static - Load is calculated at the bearing and is applied before test. It remains constant throughout the test.
Linearly Increasing - Load is time dependent starting from zero at the beginning increasing to max load at the final speed (15,000 rpm)
Ramp Rate - The rate (Revolutions per minute per sec) at which the rotor was driven to reach 15,000 rpm.
Vertical - Load is applied downward in the vertical direction.
Horizontal - Load is a side load in the horizontal direction.
Rotor Weight - This is 3.18 kg (7 lb.) at the test bearing.

The results of these tests are displayed by shaft centerline plots with several points of interest indicated on each plot. The x-y positions have the DC offset voltage subtracted and represent the outboard location of the bearing. Thus, point (0, 0) indicates the position of the rotor when it starts to rotate. Note that the rotor rotates counterclockwise. Supply pressure, recess pressure, flow, speed, and time are provided for points of interest. Exit temperature is not noted due to its insignificance. Its location during testing did not allow for accurate data since it was located too far from the actual water exiting from the bearing. All of this information helps to indicate the position of the rotor with time and helps to determine the speed when hydrostatic lift-off occurs. Hydrostatic lift-off occurs when the pressure developed in the bearing overcomes the forces acting on the rotor to

center the rotor. These shaft centerline plots were graphically interpreted to determine hydrostatic lift-off. Visual evidence of lift-off is when the rotor begins a clear change in direction towards the center of the bearing clearance. This point was then compared the pressure ratio at that point in time to verify that recess pressure was less than the supply pressure, indicating lift-off. Equation 3 defines the pressure ratio which was utilized to determine hydrostatic lift-off, specifically in the vertical direction when the load was applied on the pad.

$$P_R = \frac{\text{Recess Pressure}}{\text{Supply Pressure}} \tag{3}$$

Data obtained did not include sufficient evidence to quantify when hydrodynamic lift-off occurs. The measured results will be used to estimate when the hydrostatic lift-off of the rotor occurs. Fig. 19 shows the resulting shaft centerline for Case 1 with a 1X rotor weight static load.

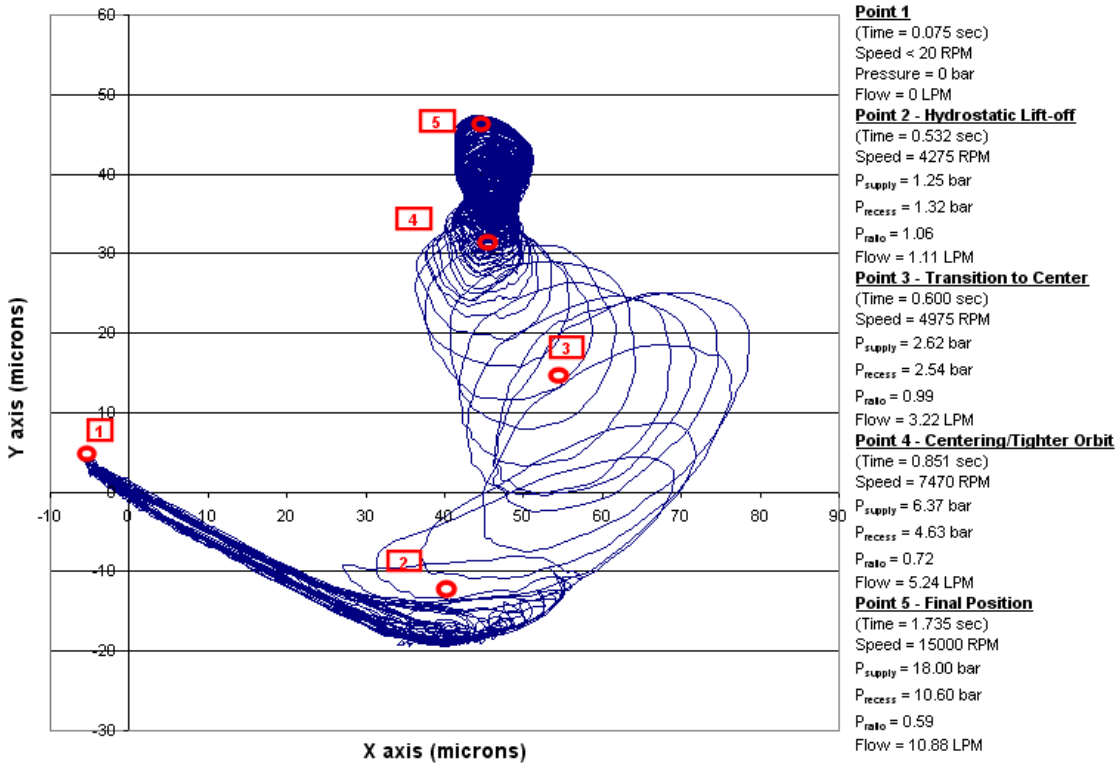

Fig. 19. Case 1 test result with 1X rotor weight static load (Supply Temp = 23.3˚ C (74˚F)).

In this shaft centerline plot, the rotor seems to start in an awkward side position, and then climbs the wall of the bearing, sticking and slipping until adequate supply pressure allows the rotor to transition to the hydrodynamic regime. Once the pressure begins to increase

significantly, and the rotor moves upward towards the center, hydrostatic lift-off occurs, which is 4275 rpm depicted by Point 2 in Fig. 19. At this point, note that the pressure ratio had just begun to reduce below 1.0, and the flow is significant at 1.11 LPM (0.29 GPM). The final position, described by Point 5, shows that the rotor is centered with a 0.59 pressure ratio.

Fig. 20 shows the resulting shaft centerline for Case 1 with an 8X rotor weight static load. The shaft centerline plot shows some severe rubbing occurring during initial start under the heavier load.

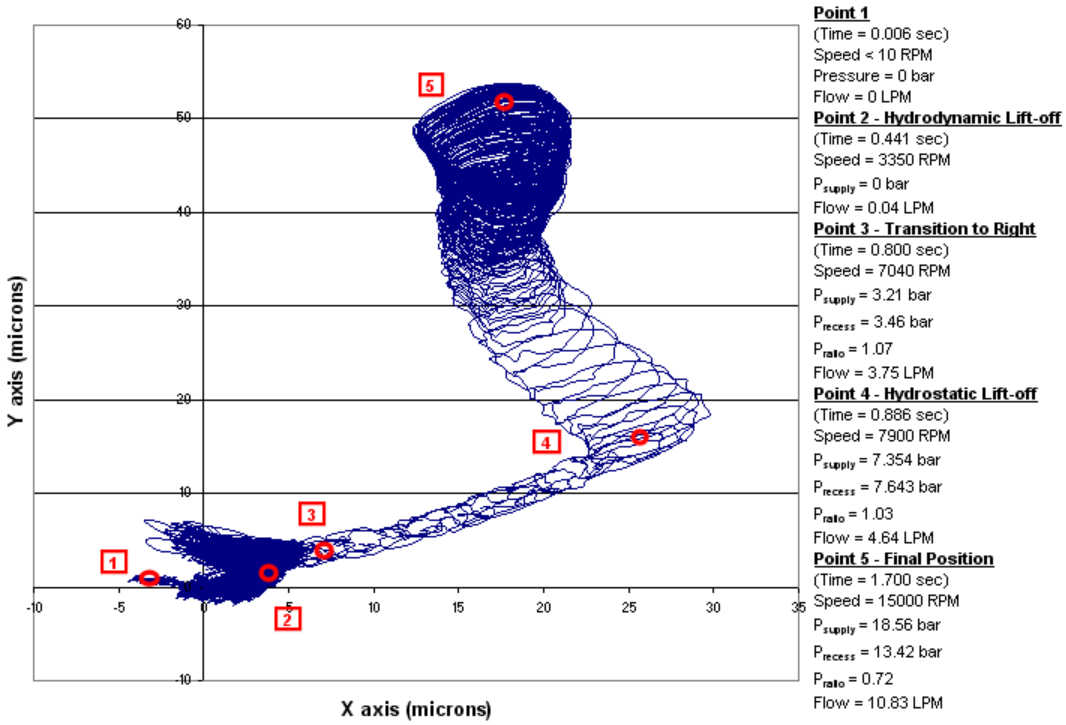

Fig. 20. Case 1 test result with 8X rotor weight static load (Supply Temp = 23.9˚ C (75˚F)).

Once the rotor sees a significant increase in pressure, it moves to the right and has a delayed hydrostatic lift-off due to the increased loading. Hydrostatic lift-off occurs at 7900 rpm, at Point 4. The center position is also 0.0127 mm (0.0005 in.) lower than the 1X loading case with a final position pressure ratio of 0.74 probably indicating a smaller clearance in the bottom pocket.

Fig. 21 shows the resulting shaft centerline for Case 6 with a 1X rotor weight static side load which corresponds to load on land as well.

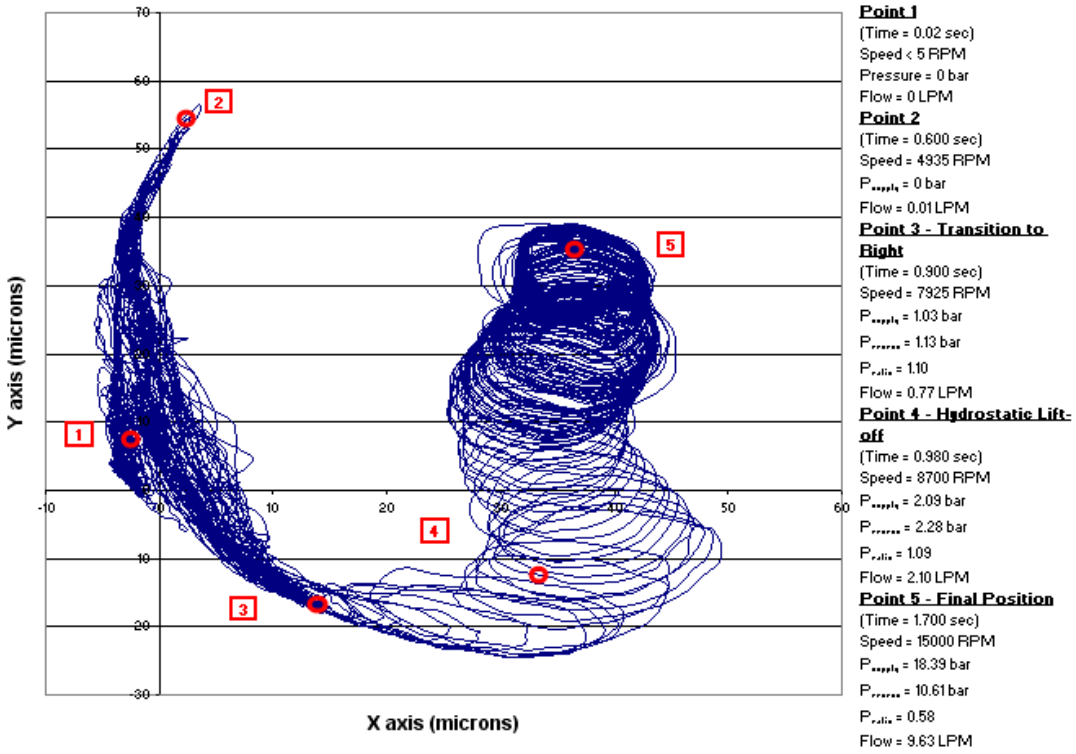

Fig. 21. Case 6 test result with 1X rotor weight static load (Supply Temp = 27.2˚C (81˚F)).

This result also shows severe rubbing initially when the rotor tried to climb the bearing surface. When the supply pressure started to increase, the bearing moved to the right and then eventually upward to center. Hydrostatic lift-off occurs at 8700 rpm, depicted by Point 4 and the transition upward. This is almost twice the lift-off speed under the same load of the first test case.

Fig. 22 describes the resulting shaft centerline for Case 6 with an 8X rotor weight static side load.

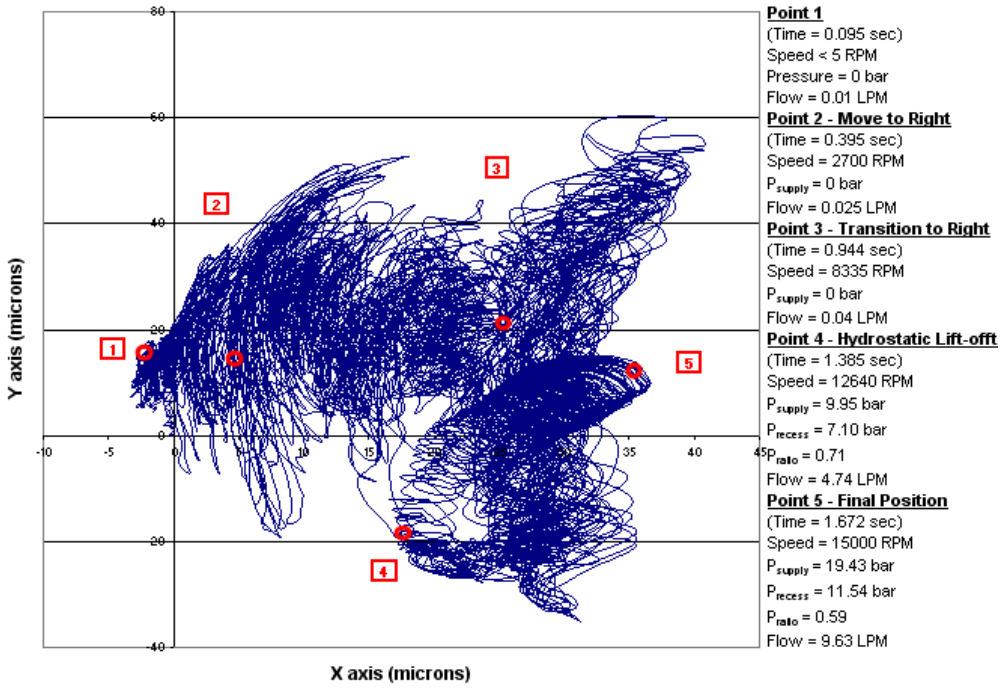

Fig. 22. Case 6 test result with 8X rotor weight static load (Supply Temp = 27.8˚C (82˚F)).

The test result shows severe rubbing and instability (an unclear orbit and irregular shaft movement) with a low supply pressure during the start-up. The rotor seems to move slowly to the right with an unclear orbit finally stabilizing with higher supply pressure of 8.03 bar (116.5 psia) when the rotor hydrostatically lifts-off at 12640 rpm, at Point 4 on the graph.

Torque is another parameter that indicates how soon the rotor lifts-off. The faster the lift-off, the smaller the drag torque will be seen. This viewpoint is verified by comparing the torques during both the 1X and 8X static load cases in the vertical direction, Fig. 23.

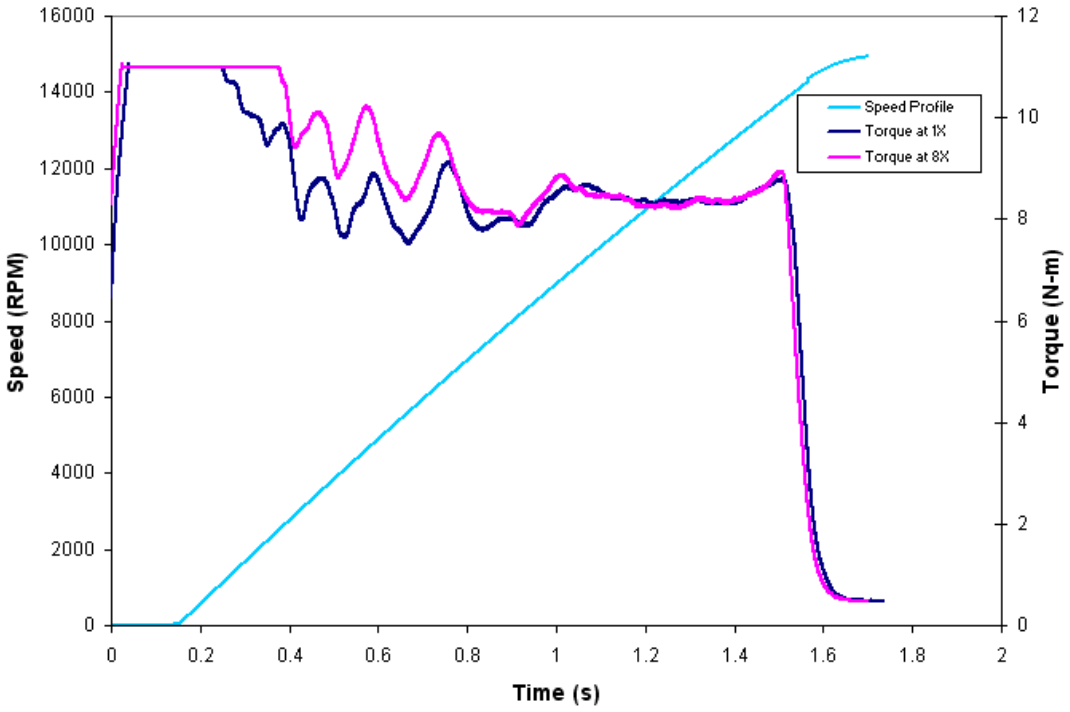

Fig. 23. Torque and speed versus time depicting the torque difference between 1X and 8X static loading.

The figure shows that the two tests have almost the exact starting torque values of 11 N-m (8.1 Ft. lbs.). Notice that the 1X case torque decreases sooner than the 8X loading case. This difference confirms that lift-off occurs sooner for more lightly loaded case. Fig. 24 takes this concept and compares the initial torque at (8824 rpm/sec) by decreasing the ramp rate to 4112 rpm/sec and 2206 rpm/sec. The start torque for the 50% torque case is almost half of the 100% case, and the start torque for the 25% case is a quarter of the 100% case; therefore, decreasing the ramp rate does in fact decrease the starting torque. It is also worth noting that the decrease in starting torque indicates an even sooner lift-off.

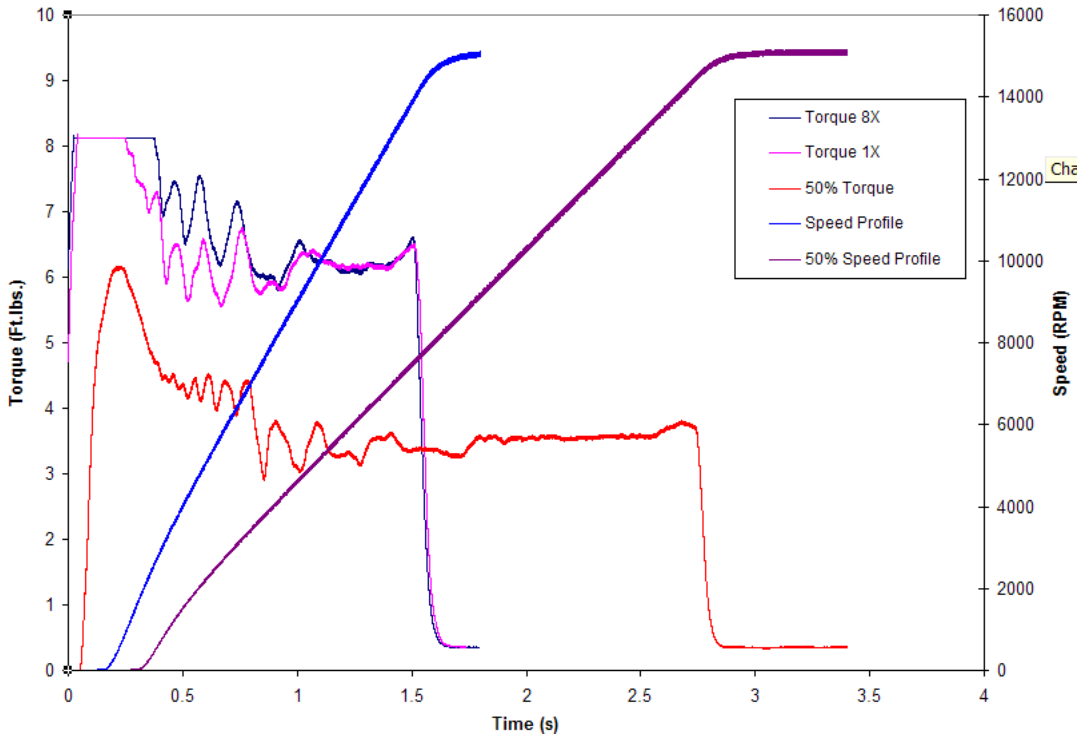

Fig. 24. Torque and speed versus time with a comparison of torque with 4412 rpm/sec ramp rate with 18.3 bar (264.7 psia) supply pressure at 15,000 rpm.

Table 6 lists the graphically determined hydrostatic lift-off speed results for all the test cases and conditions.

Table 6. Test results giving the hydrostatic lift-off speeds for test cases 1-10.

	Ramp Rate (RPM/sec)	Pressure @ 15,000 rpm	Load Orientation	Multiples of Rotor Weight Test Results (Hydrostatic Lift-off Speed (RPM))							
				1X	2X	3X	4X	5X	6X	7X	8X
Case 1	8824	18.3 bar (264.7 psia)	Load on Pad (Vertical)	4,275	5,950	6,000	6,400	6,750	6,300	7,300	7,900
Case 2	4412	18.3 bar (264.7 psia)	Load on Pad (Vertical)	3,025	4,525	3,785	5,410	4,320	4,650	6,030	6,880
Case 3	4412	9.63 bar (139.7 psia)	Load on Pad (Vertical)	2,915	8,750	9,240	7,830	8,815	9,250	11,030	11,760
Case 4	2206	9.63 bar (139.7 psia)	Load on Pad (Vertical)	3,265	2,735	4,460	4,995	8,120	8,915	10,510	11,290
Case 5	2206	5.32 bar (77.2 psia)	Load on Pad (Vertical)	2,080	4,280	6,795	8,800	9,365	10,600	13,285	14,315
Case 6	8824	18.3 bar (264.7 psia)	Load on Land (Horizontal)	N/A	8,700	11,155	10,375	12,420	11,280	11,425	12,640
Case 7	4412	18.3 bar (264.7 psia)	Load on Land (Horizontal)	N/A	7,140	8,015	8,540	9,125	10,250	11,100	11,620
Case 8	4412	9.63 bar (139.7 psia)	Load on Land (Horizontal)	N/A	7,415	8,060	9,000	9,000	9,680	11,600	12,040
Case 9	2206	9.63 bar (139.7 psia)	Load on Land (Horizontal)	N/A	4,195	4,810	5,635	7,840	8,335	10,570	11,515
Case 10	2206	5.32 bar (77.2 psia)	Load on Land (Horizontal)	N/A	4,575	7,355	8,295	9,105	11,950	14,355	14,945

Cases 1-5 represent a vertical loading condition (load on recess), while cases 6-10 represent a horizontal loading condition (load on land). The lift-off speeds for horizontal loading are much higher than the vertical load. For all cases, when the ramp rate was reduced, the lift-off speed decreased. Increasing the applied load for all cases increased

the lift-off speed. The 8X load condition with cases 5 and 10 lifted off right before reaching steady-state (15,000 rpm). When ramp rate is constant and pressure is reduced, lift off speed increases for the vertical loading which is evident in the difference in lift-off speeds in cases 2 and 3 and cases 4 and 5, but increases for the horizontal loading evident in the differences in lift-off speeds for cases 7 and 8 and 9 and 10.

With all the rubbing and high loading, the bearing and rotor did not go undamaged. After undergoing in excess of 100 start transients, Fig. 25 depicts the burnishing that occurred on the rotor.

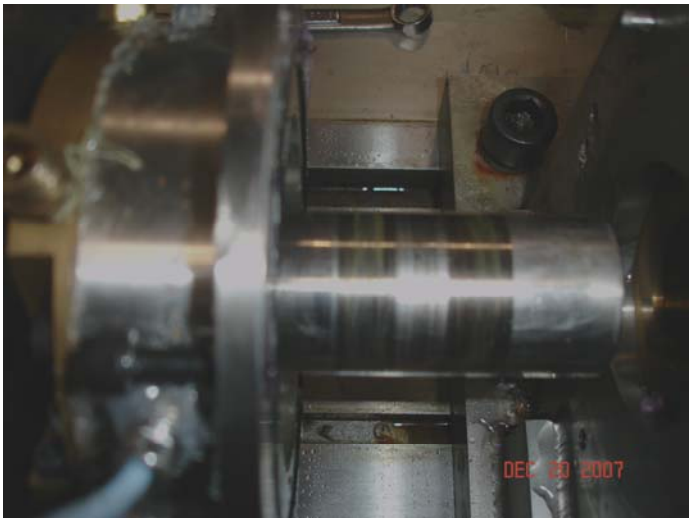

Fig. 25. Burnishing of the rotor seen after completed testing.

Heavier burnishing is present on the surface without the recess pockets. Also, small particles of bearing bronze from the test bearing are present on the rotor. Fig. 26 shows the damage to the test bearing surface with heavy burnishing and some pitting in the direction of loading.

Fig. 26. Burnishing and pitting of the test bearing after completed testing.

Fig. 27 depicts the bottom of the bearing where the vertical loading occurred. The bottom recess pocket is also visible. Heavy pitting occurred at this location since this is where the rotor started on the vertical loading cases.

Fig. 27. Localized pitting and burnishing where loading was applied during testing.

Conclusions

Hydrodynamic lift-off occurs when the rotational speed of the rotor causes the wedge of effect of the film to overcome forces acting on the rotor, while hydrostatic lift-off occurs when the pressure (which is speed dependent) developed in the bearing overcomes the forces acting on the rotor to center the rotor. The lift-off speed is an important quantity to determine for a certain condition to prevent rotor and bearing damage due to a prolonged rotor/bearing contact. Data for a lift-off code validation using water as a supply medium have been completed successfully. The data gathered here is more than adequate to help validate lift-off. The data can be accessed via a portable hard drive. Appendix A gives the directions on accessing and analyzing the data. Since the tests were recorded by .dat files, they can be replayed in LabView or sorted using other computer programs. Conclusions regarding the testing can be viewed in the following statements:

- Hydrodynamic lift-off cannot be accurately predicted with this graphical method
- Hydrostatic lift-off can be determined by graphical observation
- Hydrostatic lift-off is highly pressured dependent
- Hydrostatic lift-off increases to a higher speed for higher loads and ramp rates
- The test bearing and rotor surfaces were significantly damaged during testing
- To avoid damage during start transients, ample supply pressure must be present to avoid rotor/stator contact.

References

[1] Childs, D. and Hale, K., "A Test Apparatus and Facility to Identify the Rotordynamic Coefficients of High-Speed Hydrostatic Bearings," ASME *Journal of Tribology*, Vol. 116, n2, 1994, pp. 337-344.

[2] Scharrer, J. K., Tellier, J. and Hibbs, R., "A Study of the Transient Performance of Hydrostatic Journal Bearings: Part I-Test Apparatus and Facility," STLE Paper 91-TC-3B-1, 1991.

[3] Scharrer, J. K., Tellier, J. and Hibbs, R., "A Study of the Transient Performance of Hydrostatic Journal Bearings: Part II-Experimental Results," STLE Paper 91-TC-3B-2, 1991.

[4] Scharrer, J., Tellier, J. and Hibbs, R., "Start Transient Testing of an Annular Hydrostatic Bearing in Liquid Oxygen," AIAA Paper 92-3404, 1992.

[5] Pavelek, Dustin, "Development of a Test Apparatus for Validating Predictions of (i) Dry-Friction Whirl/Whip and (ii) Transient Hybrid Bearing Performance," 2006.

[6] Dyck, B.J., "Experimental Study of Dry-Friction Whirl and Whip for a Rotor Supported by an Annular Rub Surface," 2007.

[7] Mosher, P., and Childs, D., "Theory Versus Experiment for the Effects of Pressure Ratio on the Performance of an Orifice-Compensated Hybrid Bearing," ASME Journal of Vibration and Acoustics, 120, No. 4, October 1998, pp. 930-936.

Appendix A

Data Storage

The following describes how the test data and results are stored and how it can be accessed. The data is stored in a hierarchy of folders beginning with "Final Transient Test Results." This folder can be seen in Fig. 28

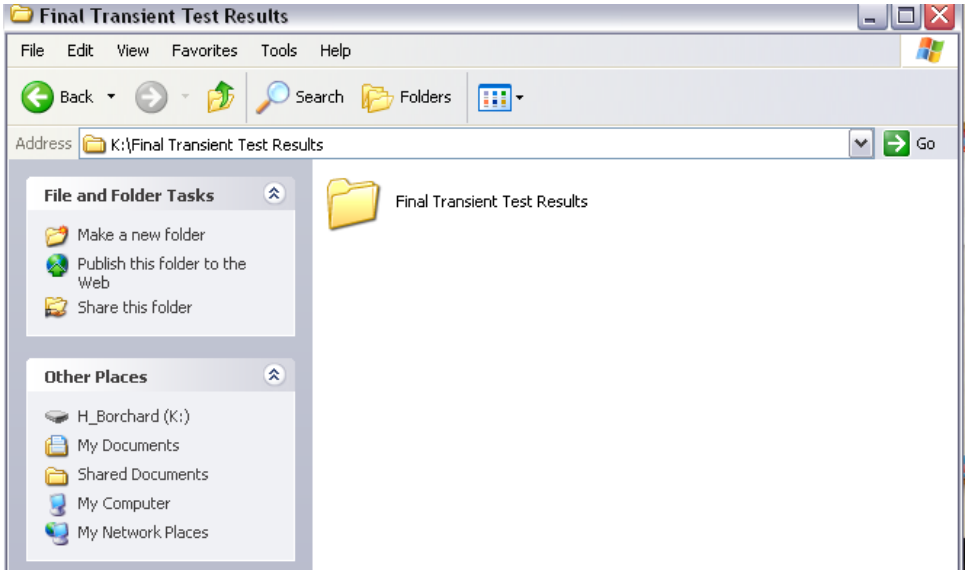

Fig. 28. First folder on the storage device.

The second hierarchy separates the results into two categories, "Static Side Loading" and "Static Vertical Loading." Fig. 29 shows this separation.

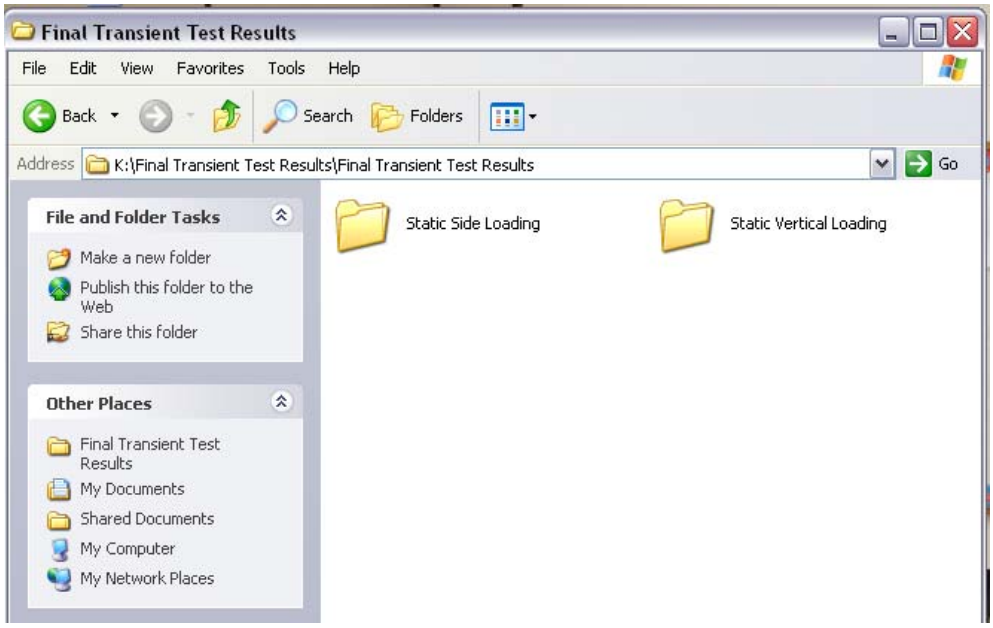

Fig. 29. Next level of folders depicting both the vertical and side loading test results.

The third hierarchy has the specific cases. Each has 5 different cases which vary the parameters of pressure and torque. Fig. 30 shows the cases listed under the "Static Side Loading" hierarchy.

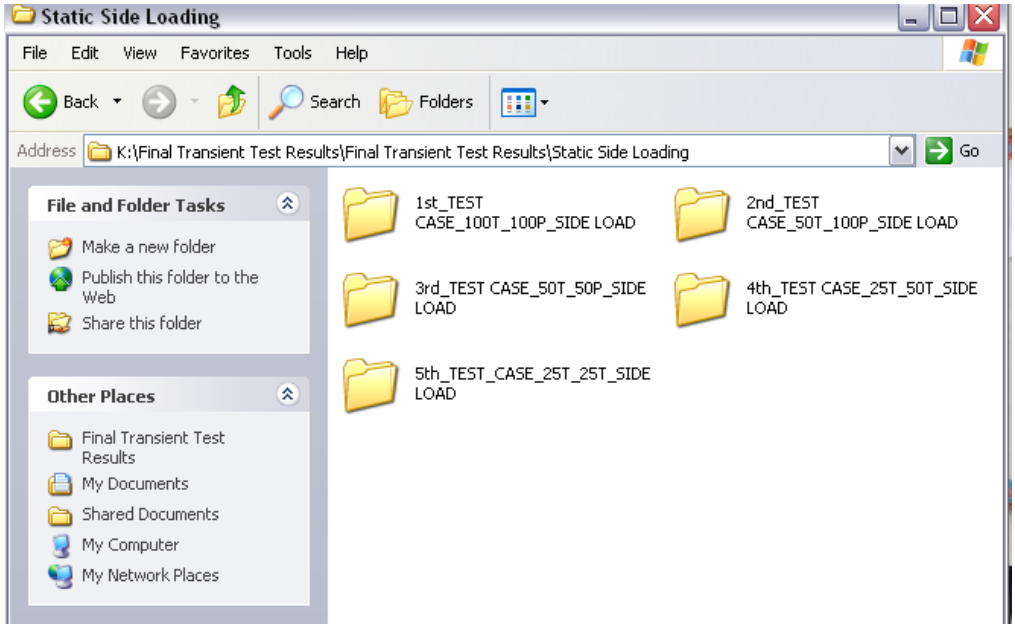

Fig. 30. The third hierarchy of folders showing the different test cases for the side loading cases.

Fig. 31 shows the cases listed under the "Static Vertical Loading" hierarchy.

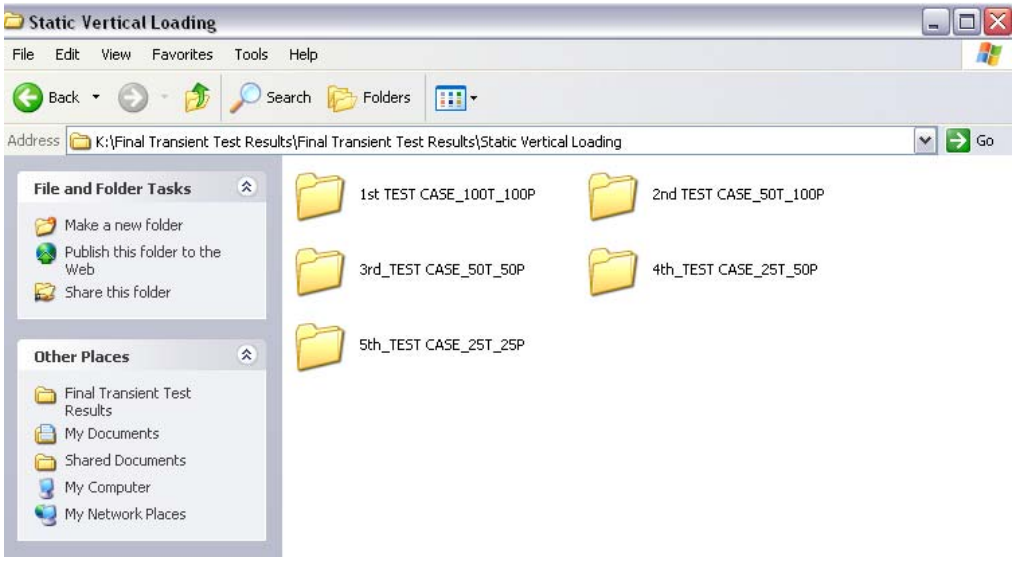

Fig. 31. The third hierarchy of folders showing the different test cases for the vertical loading cases.

The fourth hierarchy of folders gives the different loading cases described by multiples of rotor weight. Loading range varies from 1 times the rotor weight to 8 times the rotor weight. Fig. 32 shows the list of folders representing the different loading cases.

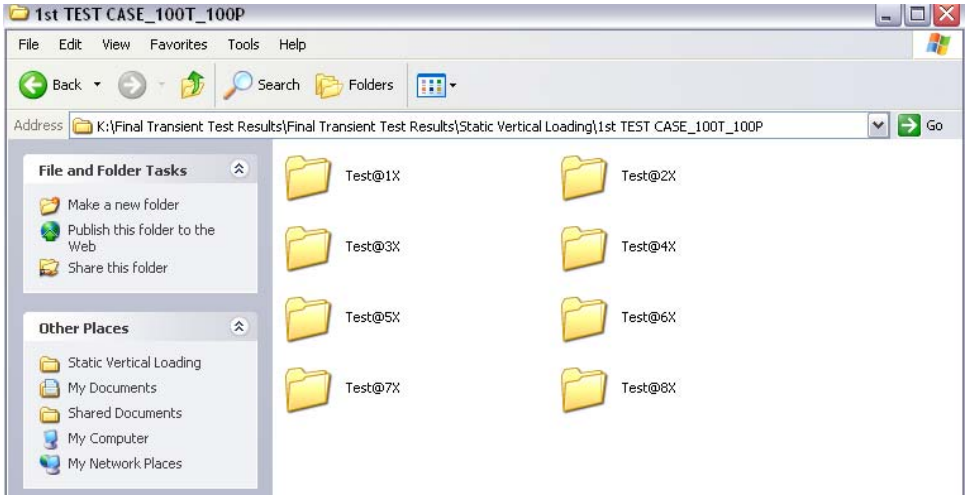

Fig. 32. Fourth hierarchy giving folders for each specific test loading condition.

The fifth and final hierarchy gives the data. Excel spreadsheets labeled "Profiles_01" and "Profiles_02" have 4 seconds worth of data of specific channels. The spreadsheets are named in numerical order based on when they occur in time. The first 4 seconds of recorded data with be in "Profile_01" and the next 4 seconds will be in "Profiles_02." A spreadsheet with the name "Profiles_01_100T_100P_1x" has a combination of the data which has been processed for results. Each file also contains a .dat file will all the

recorded channels of data and a screenshot of LabView. Fig. 33 gives the details of the actual data files.

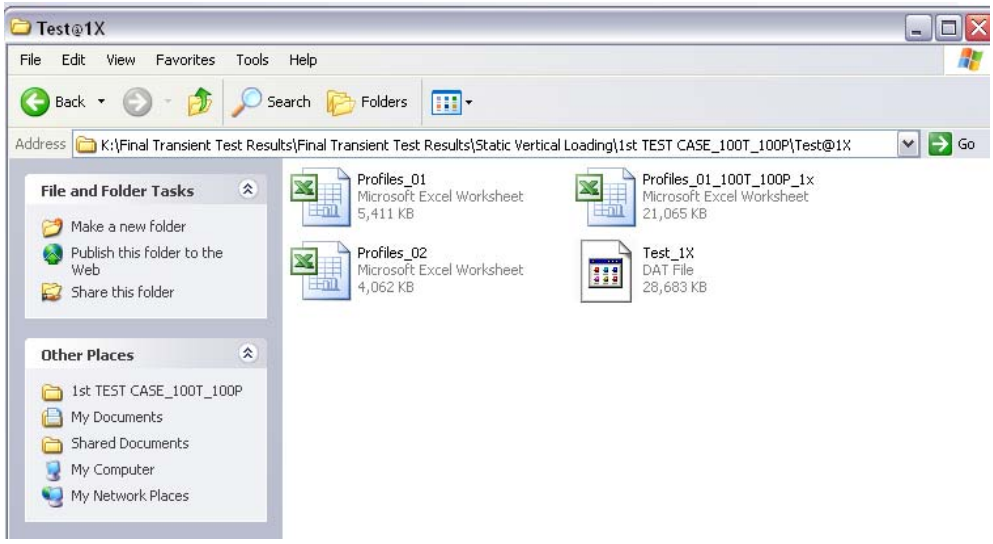

Fig. 33. The fifth and final hierarchy which consists of the test results and a .dat file of the recorded channels.

Every .dat file recorded information according to Fig. 34. Each channel is in order (top to bottom).

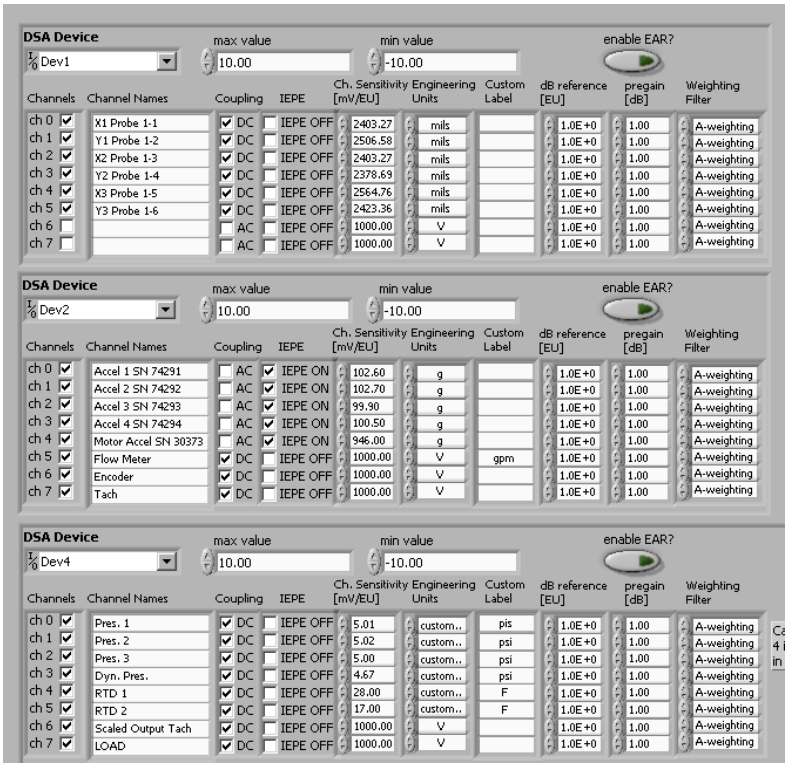

Fig. 34. The list in order of the channels recorded in the .dat file for each test.

Data Processing

Further data processing can be accomplished in with a code base program that can separate out each channel of data. When the excel file is first opened it shows 14 columns worth of data. Each row represents a snap shot in time of the test. A sample is shown on each row every 0.0002 sec (5000 Hz sampling rate). Every column has a heading as seen in Fig. 35. The X adj and Y adj takes the raw prox probe signals and rotates them into the proper axis (Test Case 1@5X is used for this example).

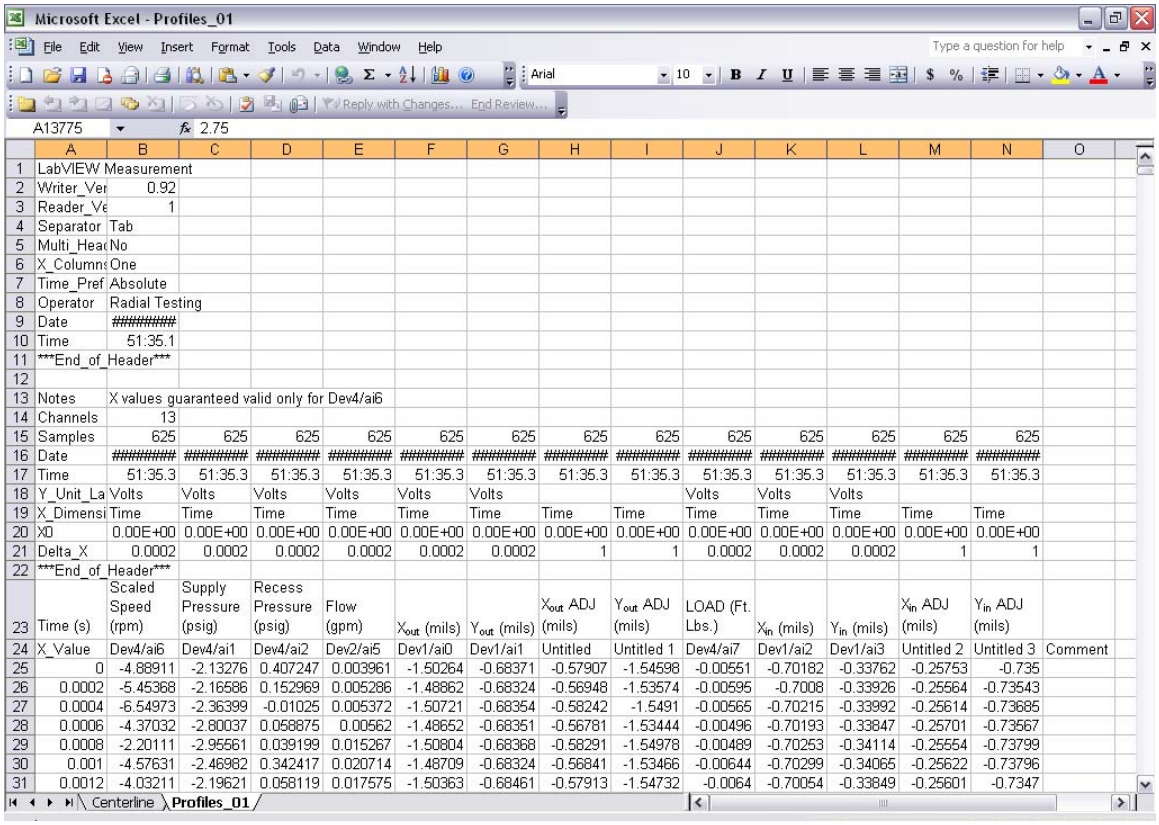

Microsoft Excel - Profiles_01

File Edit View Insert Format Tools Data Window Help

A13775 2.75

	A	B	C	D	E	F	G	H	I	J	K	L	M	N	O
1	LabVIEW Measurement														
2	Writer_Ver	0.92													
3	Reader_Ve	1													
4	Separator	Tab													
5	Multi_Hea	No													
6	X_Columns	One													
7	Time_Pref	Absolute													
8	Operator	Radial Testing													
9	Date	#########													
10	Time	51:35.1													
11	***End_of_Header***														
12															
13	Notes	X values guaranteed valid only for Dev4/ai6													
14	Channels	13													
15	Samples	625	625	625	625	625	625	625	625	625	625	625	625	625	
16	Date	#########	#########	#########	#########	#########	#########	#########	#########	#########	#########	#########	#########	#########	
17	Time	51:35.3	51:35.3	51:35.3	51:35.3	51:35.3	51:35.3	51:35.3	51:35.3	51:35.3	51:35.3	51:35.3	51:35.3	51:35.3	
18	Y_Unit_La	Volts	Volts	Volts	Volts	Volts	Volts			Volts	Volts	Volts			
19	X_Dimensi	Time	Time	Time	Time	Time	Time	Time	Time	Time	Time	Time	Time	Time	
20	X0	0.00E+00	0.00E+00	0.00E+00	0.00E+00	0.00E+00	0.00E+00	0.00E+00	0.00E+00	0.00E+00	0.00E+00	0.00E+00	0.00E+00	0.00E+00	
21	Delta_X	0.0002	0.0002	0.0002	0.0002	0.0002	0.0002	1	1	0.0002	0.0002	0.0002	1	1	
22	***End_of_Header***														
23	Time (s)	Scaled Speed (rpm)	Supply Pressure (psig)	Recess Pressure (psig)	Flow (gpm)	X_{out} (mils)	Y_{out} (mils)	X_{out} ADJ (mils)	Y_{out} ADJ (mils)	LOAD (Ft. Lbs.)	X_{in} (mils)	Y_{in} (mils)	X_{in} ADJ (mils)	Y_{in} ADJ (mils)	
24	X_Value	Dev4/ai6	Dev4/ai1	Dev4/ai2	Dev2/ai5	Dev1/ai0	Dev1/ai1	Untitled	Untitled 1	Dev4/ai7	Dev1/ai2	Dev1/ai3	Untitled 2	Untitled 3	Comment
25	0	-4.88911	-2.13276	0.407247	0.003961	-1.50264	-0.68371	-0.57907	-1.54598	-0.00551	-0.70182	-0.33762	-0.25753	-0.735	
26	0.0002	-5.45368	-2.16586	0.152969	0.005286	-1.48862	-0.68324	-0.56948	-1.53574	-0.00595	-0.7008	-0.33926	-0.25564	-0.73543	
27	0.0004	-6.54973	-2.36399	-0.01025	0.005372	-1.50721	-0.68354	-0.58242	-1.5491	-0.00565	-0.70215	-0.33992	-0.25614	-0.73685	
28	0.0006	-4.37032	-2.80037	0.058875	0.00562	-1.48652	-0.68351	-0.56781	-1.53444	-0.00496	-0.70193	-0.33847	-0.25701	-0.73567	
29	0.0008	-2.20111	-2.95561	0.039199	0.015267	-1.50804	-0.68368	-0.58291	-1.54978	-0.00489	-0.70253	-0.34114	-0.25554	-0.73799	
30	0.001	-4.57631	-2.46982	0.342417	0.020714	-1.48709	-0.68324	-0.56841	-1.53466	-0.00644	-0.70299	-0.34065	-0.25622	-0.73796	
31	0.0012	-4.03211	-2.19621	0.058119	0.017575	-1.50363	-0.68461	-0.57913	-1.54732	-0.0064	-0.70054	-0.33849	-0.25601	-0.7347	

Centerline | Profiles_01

Fig. 35. Test results in excel (specific channels were chosen to record to excel during testing for data processing).

The first step in finding the lift-off speed is to find the first point at which the rotor starts moving. This is done by plotting an X/Y scatter plot for Columns H and I. Fig. 36 shows the result of this plot.

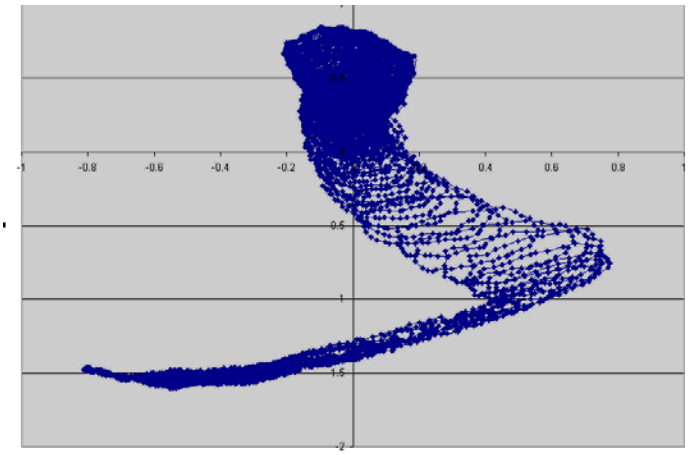

Fig. 36. Raw X vs. Y data resulting in shaft centerline.

This plot represents the shaft movement from 0 – 15,000 rpm. The plot range is manipulated to locate the point when the rotor first begins to move.

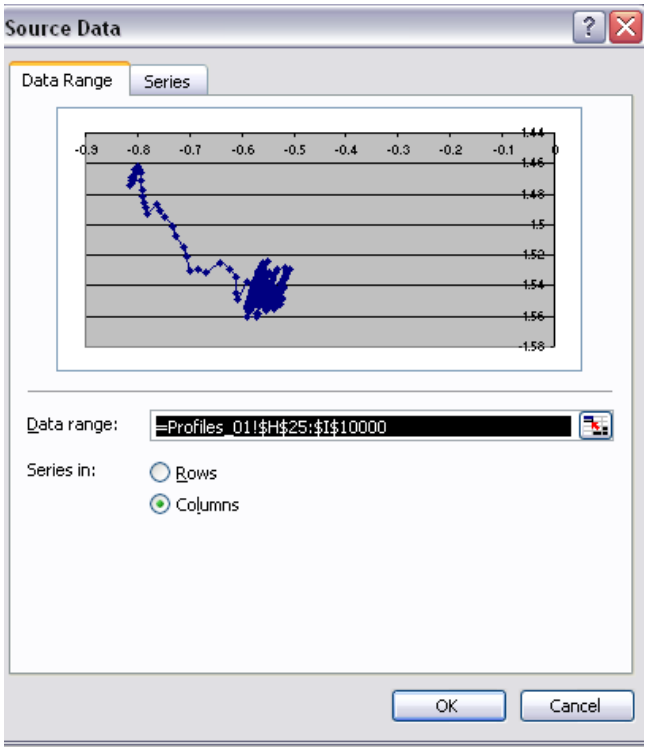

Fig. 37. Data range configuration in excel.

Every excel spreadsheet recorded 20024 rows worth of data (4 sec of data points). The data range is reduced from 25-20024 to 25-10000 to reduce the amount of data points in the plotting range.

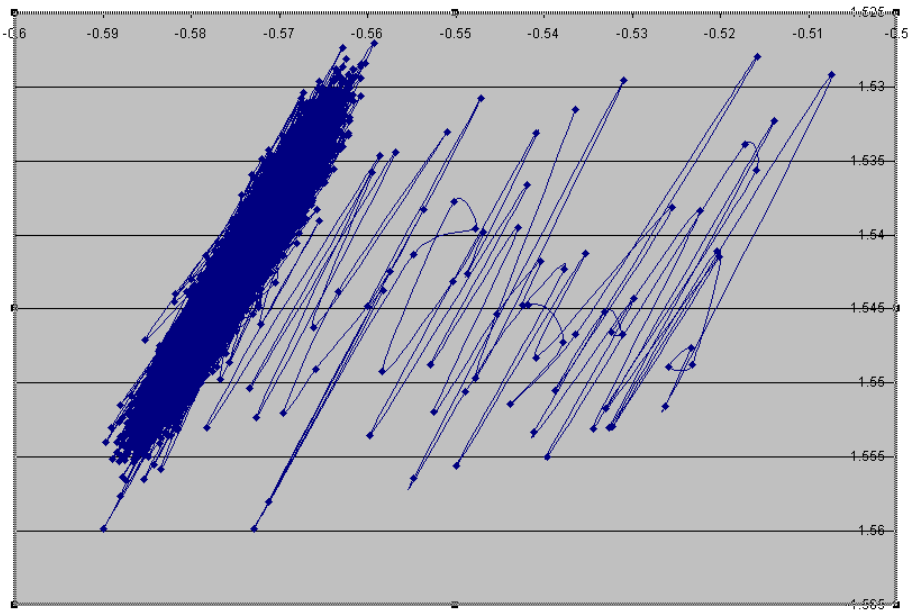

Fig. 38. Point at which rotor begins to rotate.

Fig. 38 shows the first movement of the rotor. The dark area represents the initial shaft position that will need to be subtracted out of the X adj and Y adj to bring the centerline to (0,0). After further reduction in the data range the first data point was found to be row number 9878. Another row is added to separate the initial data from the actual test data. Row number 9878 is highlighted in Fig. 39 and is the first data point. The time value in Column B and Row 9878 is used to offset the rest of the time points in a new Column A.

	A	B	C	D	E	F	G	H	I	J	K	L	M	N	O
23	New Time (s)	Time (s)	Scaled Speed (rpm)	Supply Pressure (psig)	Recess Pressure (psig)	Flow (gpm)	X_{out} (mils)	Y_{out} (mils)	X_{out} ADJ (mils)	Y_{out} ADJ (mils)	LOAD (Ft. Lbs.)	X_{in} (mils)	Y_{in} (mils)	X_{in} ADJ (mils)	Y_{in} ADJ (mils)
24		X_Value	Dev4/ai6	Dev4/ai1	Dev4/ai2	Dev2/ai5	Dev1/ai0	Dev1/ai1	Untitled	Untitled 1	Dev4/ai7	Dev1/ai2	Dev1/ai3	Untitled 2	Untitled 3
9863		1.9676	2.760366	-1.61136	0.810107	0.020846	-1.4905	-0.68304	-0.57096	-1.53693	4.120066	-0.70098	-0.33825	-0.25649	-0.73484
9864		1.9678	2.310239	-1.27204	0.840882	0.019532	-1.48681	-0.6834	-0.5681	-1.53457	4.134665	-0.69998	-0.33944	-0.25494	-0.73496
9865		1.968	-0.3803	-1.49073	1.001825	0.016755	-1.51041	-0.68551	-0.58329	-1.55275	4.188081	-0.70104	-0.33745	-0.2571	-0.73432
9866		1.9682	2.472997	-1.4654	0.962725	0.010695	-1.48485	-0.68562	-0.56514	-1.53475	4.17716	-0.70199	-0.33898	-0.25669	-0.73608
9867		1.9684	-1.50686	-1.77889	1.291166	0.005186	-1.50928	-0.6838	-0.58371	-1.55074	4.235119	-0.69978	-0.33929	-0.25491	-0.73473
9868		1.9686	1.936425	-1.04858	1.146875	0.006459	-1.48232	-0.68548	-0.56345	-1.53287	4.247896	-0.70119	-0.33717	-0.2574	-0.73424
9869		1.9688	-2.57241	-1.2274	0.649164	0.002488	-1.508	-0.68346	-0.58304	-1.54959	4.265489	-0.7017	-0.33924	-0.2563	-0.73608
9870		1.969	1.453236	-1.11329	1.017465	-0.00089	-1.47804	-0.68491	-0.56083	-1.52944	4.322075	-0.70067	-0.34129	-0.25413	-0.73678
9871		1.9692	0.652187	-1.86742	0.779583	-0.00244	-1.50894	-0.68557	-0.58221	-1.55175	4.308537	-0.70178	-0.33897	-0.25655	-0.73592
9872		1.9694	-1.44837	-1.33223	0.719293	-0.00235	-1.48898	-0.68369	-0.56942	-1.53631	4.366828	-0.70041	-0.33965	-0.2551	-0.73544
9873		1.9696	0.125766	-1.09698	0.891335	-0.00124	-1.50949	-0.68702	-0.58157	-1.55317	4.376875	-0.701	-0.34112	-0.25448	-0.73689
9874		1.9698	-2.04345	-0.74738	1.149901	0.001894	-1.49222	-0.68538	-0.57052	-1.5398	4.394223	-0.70008	-0.34059	-0.2542	-0.73588
9875		1.97	2.849363	-0.9741	1.463965	0.003958	-1.49693	-0.68693	-0.57276	-1.54423	4.445788	-0.69948	-0.33973	-0.25438	-0.73483
9876		1.9702	1.773667	-0.55377	1.37744	0.003701	-1.49101	-0.68763	-0.56808	-1.54053	4.437656	-0.70031	-0.34167	-0.2536	-0.7368
9877															
9878	0	1.9704	-1.12541	-0.38624	1.53485	0.017491	-1.49271	-0.68704	-0.5697	-1.54132	4.496191	-0.69994	-0.34415	-0.25158	-0.73826
9879	0.0002	1.9706	0.336841	-0.47828	1.355999	0.026752	-1.49769	-0.68869	-0.57205	-1.546	4.506079	-0.69803	-0.34284	-0.25116	-0.73601
9880	0.0004	1.9708	4.377738	-0.03588	1.685269	0.026225	-1.48809	-0.68846	-0.56542	-1.53905	4.528867	-0.69862	-0.34279	-0.25161	-0.73638
9881	0.0006	1.971	1.041275	-0.0745	1.450849	0.008624	-1.50703	-0.68928	-0.57824	-1.55303	4.578615	-0.69777	-0.34291	-0.25093	-0.73587
9882	0.0008	1.9712	6.379113	-0.29771	1.467496	0.002655	-1.48013	-0.69024	-0.55854	-1.53468	4.571315	-0.69718	-0.34424	-0.24957	-0.7364
9883	0.001	1.9714	1.83979	-0.1683	1.167811	0.000419	-1.5017	-0.69085	-0.57336	-1.55037	4.630492	-0.69858	-0.34536	-0.24977	-0.73818
9884	0.0012	1.9716	-4.42119	-0.59741	1.32724	-0.00297	-1.47871	-0.69126	-0.5568	-1.5344	4.641428	-0.69728	-0.34471	-0.24931	-0.73679
9885	0.0014	1.9718	-9.1131	-0.80832	1.07271	-0.00104	-1.50254	-0.69273	-0.57262	-1.55229	4.668375	-0.69646	-0.34487	-0.24862	-0.73633
9886	0.0016	1.972	-8.42903	-0.64706	1.063627	0.002101	-1.48163	-0.69034	-0.55953	-1.53581	4.715457	-0.69662	-0.3473	-0.24701	-0.73817
9887	0.0018	1.9722	-8.78761	-1.06839	0.875695	0.005963	-1.4937	-0.69309	-0.56611	-1.54629	4.71433	-0.69604	-0.34724	-0.24663	-0.73771
9888	0.002	1.9724	-5.51216	-0.50913	1.008636	0.009016	-1.47364	-0.69439	-0.55101	-1.53303	4.773151	-0.69562	-0.34703	-0.24649	-0.73729
9889	0.0022	1.9726	-14.4967	-1.35831	1.018726	0.010473	-1.49	-0.69327	-0.56337	-1.54381	4.779846	-0.6957	-0.34662	-0.24684	-0.73703
9890	0.0024	1.9728	-7.79836	-0.82462	1.144856	0.013628	-1.50022	-0.69469	-0.56959	-1.55203	4.807887	-0.6957	-0.34722	-0.24642	-0.73746
9891	0.0026	1.973	-3.40143	-1.18777	0.925895	0.025885	-1.49546	-0.69525	-0.56583	-1.54906	4.853119	-0.69484	-0.34818	-0.24513	-0.73753

Centerline / Initial Rotor Rotation / **Profiles 01**

Fig. 39. Zero time reference representing the beginning of the test.

To zero centerline and subtract out the initial rotor position, two more columns are added and an average of the static rotor position is taken and subtracted out of the new columns. This result can be seen in Fig. 40.

H	I	J	K	L	M	N	O	P	
(mils)	X_{out} ADJ (mils)	Y_{out} ADJ (mils)			LOAD (Ft. Lbs.)	X_{in} (mils)	Y_{in} (mils)	X_{in} ADJ (mils)	Y (
/ai1	Untitled	Untitled 1			Dev4/ai7	Dev1/ai2	Dev1/ai3	Untitled 2	U
8304	-0.57096	-1.53693			4.120066	-0.70098	-0.33825	-0.25649	
.6834	-0.5681	-1.53457			4.134665	-0.69998	-0.33944	-0.25494	
8551	-0.58329	-1.55275			4.188081	-0.70104	-0.33745	-0.2571	
8562	-0.56514	-1.53475			4.17716	-0.70199	-0.33898	-0.25669	
.6838	-0.58371	-1.55074			4.235119	-0.69978	-0.33929	-0.25491	
8548	-0.56345	-1.53287			4.247896	-0.70119	-0.33717	-0.2574	
8346	-0.58304	-1.54959			4.265489	-0.7017	-0.33924	-0.2563	
8491	-0.56083	-1.52944			4.322075	-0.70067	-0.34129	-0.25413	
8557	-0.58221	-1.55175			4.308537	-0.70178	-0.33897	-0.25655	
8369	-0.56942	-1.53631			4.366828	-0.70041	-0.33965	-0.2551	
8702	-0.58157	-1.55317			4.376875	-0.701	-0.34112	-0.25448	
8538	-0.57052	-1.5398			4.394223	-0.70008	-0.34059	-0.2542	
8693	-0.57276	-1.54423	AVG X	AVG Y	4.445788	-0.69948	-0.33973	-0.25438	
8763	-0.56808	-1.54053	-0.57475	-1.54245	4.437656	-0.70031	-0.34167	-0.2536	
8704	-0.5697	-1.54132	0.005053	0.001132	4.496191	-0.69994	-0.34415	-0.25158	
8869	-0.57205	-1.546	0.002702	-0.00355	4.506079	-0.69803	-0.34284	-0.25116	
8846	-0.56542	-1.53905	0.00933	0.003394	4.528867	-0.69862	-0.34279	-0.25161	
8928	-0.57824	-1.55303	-0.00349	-0.01058	4.578615	-0.69777	-0.34291	-0.25093	
9024	-0.55854	-1.53468	0.016212	0.00777	4.571315	-0.69718	-0.34424	-0.24957	

Fig. 40. Average of the zero position of the rotor that is subtracted out to zero the prox probes.

Now the data points from the end of the test need to be truncated (the point at which the rotor reaches 15,000 rpm). This occurs at 1.7 seconds for this case due to the ramp rate. A new shaft centerline plot is generated shown if Fig. 41. This is the rough shaft centerline for the test.

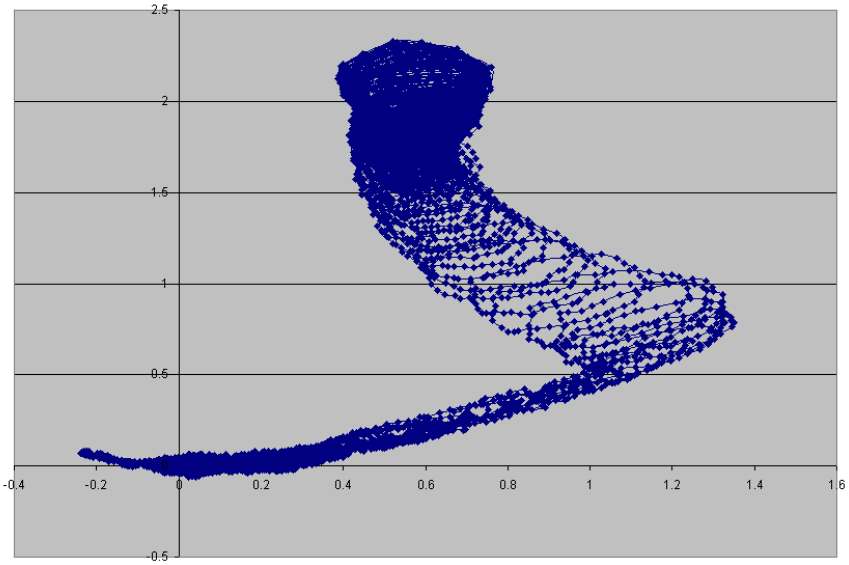

Fig. 41. New shaft centerline starting at (0,0).

Now that the full test range is narrowed down. It is possible to locate important points on the shaft centerline and have location, pressures, speed, and time with each point. To

locate hydrostatic lift-off, the data range is reduced to the point at which the shaft centerline moves up and to the center of the bearing clearance. Fig. 42 illustrates the point at which the rotor is lifting off.

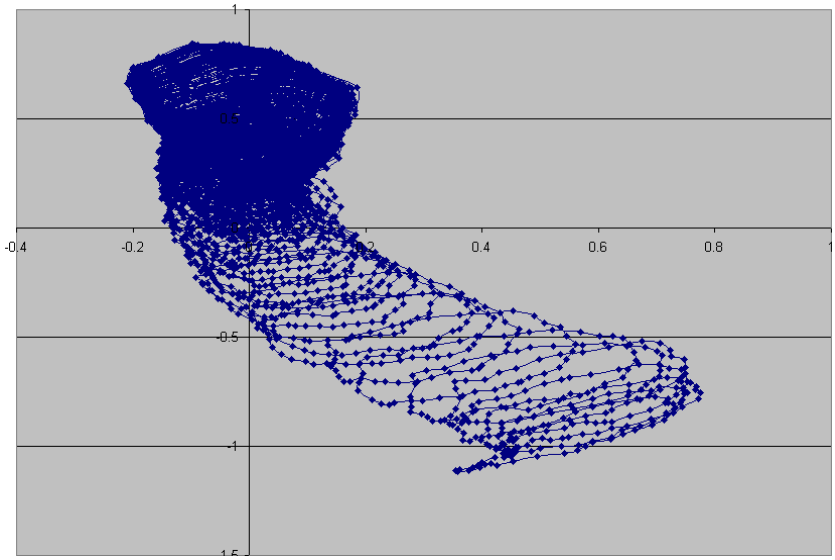

Fig. 42. Part of the shaft centerline depicting hydrostatic lift-off.

Important points to follow for data processing:

- Data points are sporadic, points must be averaged at least 10 points before and after to receive a good data point.
- The speed output from the encoder is also sporadic; a least squares approximation can be used to approximate the speed and pressure profiles.
- For longer tests, data points from “Profiles_01”, “Profiles_02”, and “Profiles_03” may need to be combined for data processing.

ROCETS SIMULATION DATA

Table 7. ROCETS data that was used as a baseline reference for the lift-off testing.

TIME (s)	PTFPAD (PSIA) (Recess Pressure)	PTFPBD (PSIA) (Supply Pressure)	SNROTF (RPM) (Speed)	TIME (s)	PTFPAD (PSIA) (Recess Pressure)	PTFPBD (PSIA) (Supply Pressure)	SNROTF (RPM) (Speed)	TIME (s)	PTFPAD (PSIA) (Recess Pressure)	PTFPBD (PSIA) (Supply Pressure)	SNROTF (RPM) (Speed)
0.00	28.00	28.00	0.10	0.49	30.33	33.20	3525.00	0.97	39.71	54.50	7947.00
0.01	28.00	28.00	0.10	0.50	30.46	33.50	3620.00	0.98	40.01	55.17	8047.00
0.02	28.00	28.00	0.10	0.51	30.58	33.77	3709.00	0.99	40.34	55.92	8159.00
0.03	28.00	28.00	0.10	0.52	30.71	34.06	3799.00	1.00	40.68	56.69	8272.00
0.04	27.94	27.88	0.10	0.53	30.85	34.36	3890.00	1.01	41.03	57.47	8386.00
0.05	28.00	28.01	0.10	0.54	30.98	34.67	3981.00	1.02	41.38	58.28	8501.00
0.06	26.56	25.99	0.10	0.55	31.12	34.96	4067.00	1.03	41.75	59.10	8617.00
0.07	22.12	19.95	0.10	0.56	31.26	35.27	4153.00	1.05	42.12	59.95	8734.00
0.08	21.41	19.06	0.10	0.57	31.39	35.58	4240.00	1.06	42.51	60.81	8853.00
0.09	21.30	18.87	0.10	0.58	31.53	35.90	4328.00	1.07	42.90	61.70	8973.00
0.10	21.13	18.59	0.10	0.59	31.68	36.22	4418.00	1.08	43.30	62.60	9094.00
0.11	21.03	18.27	52.40	0.60	31.82	36.56	4508.00	1.09	43.71	63.53	9217.00
0.12	21.03	18.00	130.80	0.61	31.97	36.88	4592.00	1.10	44.14	64.48	9341.00
0.13	21.15	17.95	209.90	0.62	32.11	37.21	4677.00	1.11	44.57	65.46	9467.00
0.14	21.39	18.10	286.50	0.63	32.26	37.56	4763.00	1.12	45.02	66.46	9594.00
0.15	21.58	18.26	359.30	0.64	32.42	37.91	4851.00	1.13	45.47	67.49	9723.00
0.16	21.76	18.42	428.50	0.65	32.58	38.28	4939.00	1.14	45.94	68.54	9854.00
0.17	21.92	18.58	494.70	0.66	32.74	38.65	5029.00	1.15	46.42	69.62	9987.00
0.18	22.08	18.74	558.00	0.67	32.90	39.01	5112.00	1.16	46.92	70.73	10120.00
0.19	22.24	18.89	618.50	0.68	33.06	39.37	5196.00	1.17	47.43	71.87	10260.00
0.20	22.37	19.05	676.60	0.69	33.22	39.75	5282.00	1.18	47.95	73.05	10400.00
0.21	22.49	19.20	732.50	0.70	33.39	40.13	5368.00	1.19	48.49	74.25	10540.00
0.22	22.74	19.52	786.60	0.71	33.57	40.53	5456.00	1.20	49.04	75.49	10680.00
0.23	23.05	19.91	840.00	0.72	33.74	40.94	5543.00	1.21	49.61	76.76	10820.00
0.24	23.33	20.26	893.10	0.73	33.92	41.35	5631.00	1.22	50.20	78.07	10970.00
0.25	28.18	28.39	988.00	0.74	34.11	41.76	5719.00	1.23	50.80	79.41	11120.00
0.26	28.21	28.47	1106.00	0.75	34.30	42.19	5807.00	1.24	51.42	80.79	11270.00
0.27	28.27	28.59	1222.00	0.76	34.49	42.63	5895.00	1.25	52.06	82.22	11420.00
0.28	28.32	28.71	1338.00	0.77	34.68	43.07	5984.00	1.26	52.72	83.69	11580.00
0.29	28.38	28.84	1454.00	0.78	34.88	43.52	6073.00	1.27	53.40	85.20	11740.00
0.30	28.44	28.99	1569.00	0.79	35.08	43.98	6162.00	1.28	54.10	86.76	11900.00
0.31	28.51	29.15	1681.00	0.80	35.28	44.44	6251.00	1.29	54.83	88.36	12070.00
0.32	28.59	29.31	1792.00	0.81	35.49	44.92	6341.00	1.30	55.58	90.02	12230.00
0.33	28.66	29.48	1899.00	0.82	35.70	45.40	6431.00	1.31	56.35	91.74	12410.00
0.34	28.74	29.65	2009.00	0.83	35.92	45.89	6522.00	1.32	57.15	93.51	12580.00
0.35	28.82	29.84	2115.00	0.84	36.14	46.39	6613.00	1.33	57.98	95.35	12760.00
0.36	28.91	30.03	2222.00	0.85	36.36	46.90	6704.00	1.34	58.85	97.24	12940.00
0.37	29.00	30.24	2332.00	0.86	36.59	47.42	6796.00	1.35	59.74	99.21	13130.00
0.38	29.09	30.45	2437.00	0.87	36.82	47.95	6889.00	1.36	60.66	101.20	13320.00
0.39	29.20	30.68	2543.00	0.88	37.06	48.49	6982.00	1.37	61.62	103.40	13510.00
0.40	29.29	30.90	2644.00	0.89	37.30	49.04	7075.00	1.38	62.62	105.50	13710.00
0.41	29.40	31.14	2746.00	0.90	37.55	49.60	7170.00	1.39	63.66	107.80	13920.00
0.42	29.51	31.38	2850.00	0.91	37.80	50.17	7264.00	1.40	64.73	110.20	14130.00
0.43	29.62	31.62	2948.00	0.92	38.06	50.75	7360.00	1.41	65.85	112.60	14340.00
0.44	29.73	31.87	3046.00	0.92	38.32	51.35	7456.00	1.42	67.02	115.20	14560.00
0.45	29.85	32.13	3145.00	0.93	38.59	51.95	7553.00	1.43	68.23	117.80	14780.00
0.46	29.97	32.40	3245.00	0.94	38.86	52.57	7650.00	1.44	69.49	120.50	15010.00
0.47	30.09	32.66	3338.00	0.95	39.14	53.20	7748.00				
0.48	30.20	32.93	3431.00	0.96	39.42	53.84	7847.00				

Amps Applied with MBScope

Force diagrams were used to calculate the force at the test bearing. This assumes that the weight of the rotor acts at the same location at the magnetic bearing applied load (not a calculated center of gravity).

Vertical Case

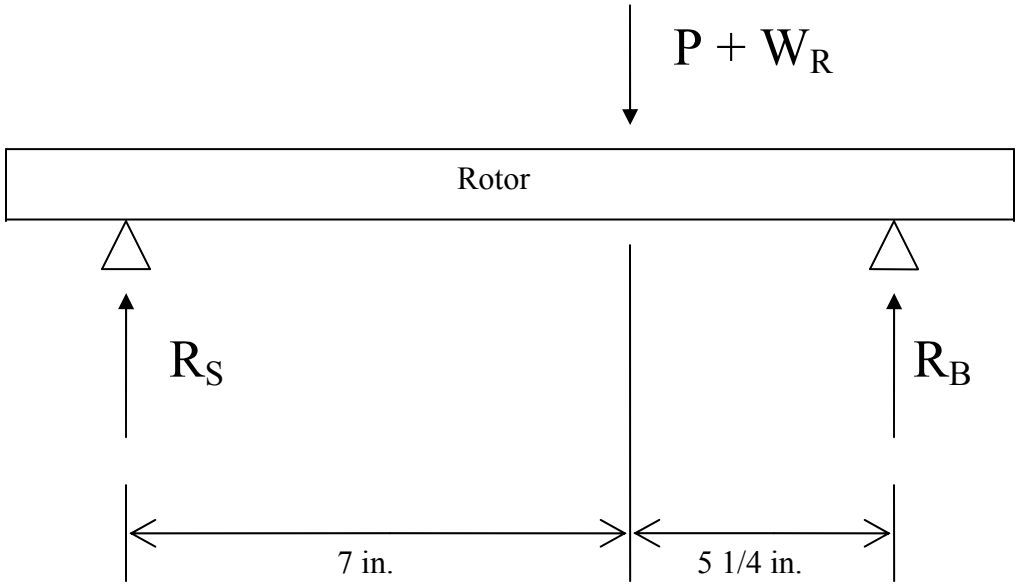

P = Applied load of Magnetic Bearing

R_S = Reaction at the Support Bearing

R_B = Reaction at the Test Bearing

W_R = Weight of the Rotor (15 lbs.)

Sum of Forces in Y-Direction

$\Sigma F_Y = P + W_R - R_S - R_B = 0$

$R_S = P + W_R - R_B$

Sum of Moments about Applied Load Location

$\Sigma M_P = R_S(7) - R_B(5.25) = 0$

$(P + W_R - R_B)7 - R_B(5.25) = 0$

$R_B = (7P - 105)/12.25$

The above relationship was used to correlate the amount of amps to use in MBScope for the Y-Direction.

Amps for Vertical Load Case

1X – 0.0 Amps
2X – 2.1 Amps
3X – 3.0 Amps
4X – 3.8 Amps
5X – 4.5 Amps
6X – 5.1 Amps
7X – 5.7 Amps
8X – 6.2 Amps

Horizontal Case

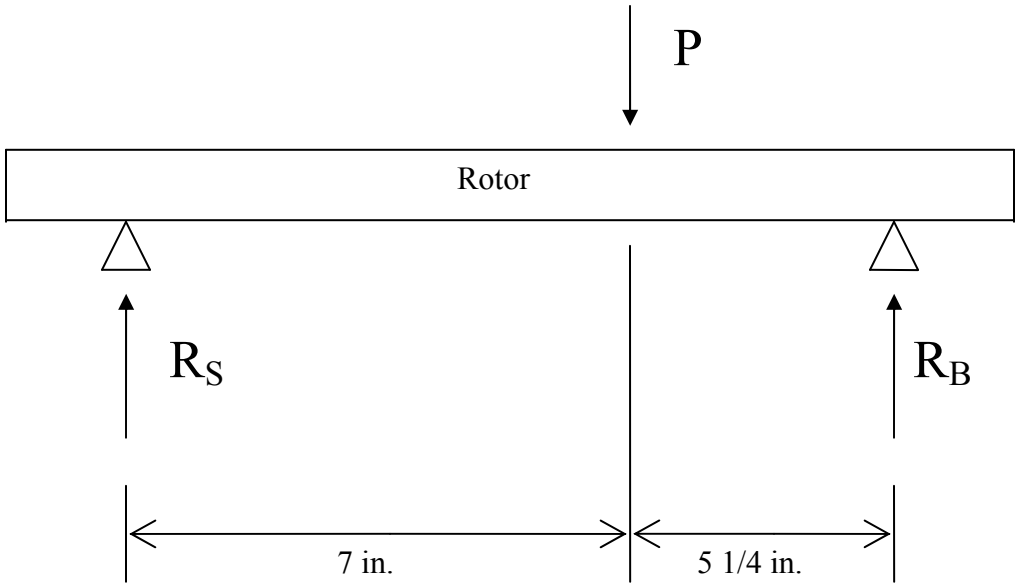

P = Applied load of Magnetic Bearing
R_S = Reaction at the Support Bearing
R_B = Reaction at the Test Bearing

Sum of Forces in Y-Direction
$\Sigma F_Y = P - R_S - R_B = 0$

Sum of Moments about Test Bearing Location
$\Sigma M_B = P(5.25) - R_S(12.25) = 0$

$R_S = 3P/7$

$P - R_B - (3P/7) = 0$

$R_B = 4P/7$

The above relationship was used to correlate the amount of amps to use in MBScope for the X-Direction.

Amps for Horizontal Load Case

2X – 3.15 Amps
3X – 4.0 Amps
4X – 4.73 Amps
5X – 5.38 Amps
6X – 5.97 Amps
7X – 7.1 Amps
8X – 7.67 Amps

LabView

LabView was used to capture the test data including prox probes, acceleration, pressure, temperature, and speed. The front panel in the Transient.vi is shows the user interface. The user inputs the test speed of the rotor, acceleration rate, and the name and location of the excel file the data writes to. Several graphs are present giving live data of the shaft centerline plot, acceleration vs. time, and x and y displacement. Fig. 43 shows the front panel that the user interfaces with to run the tests.

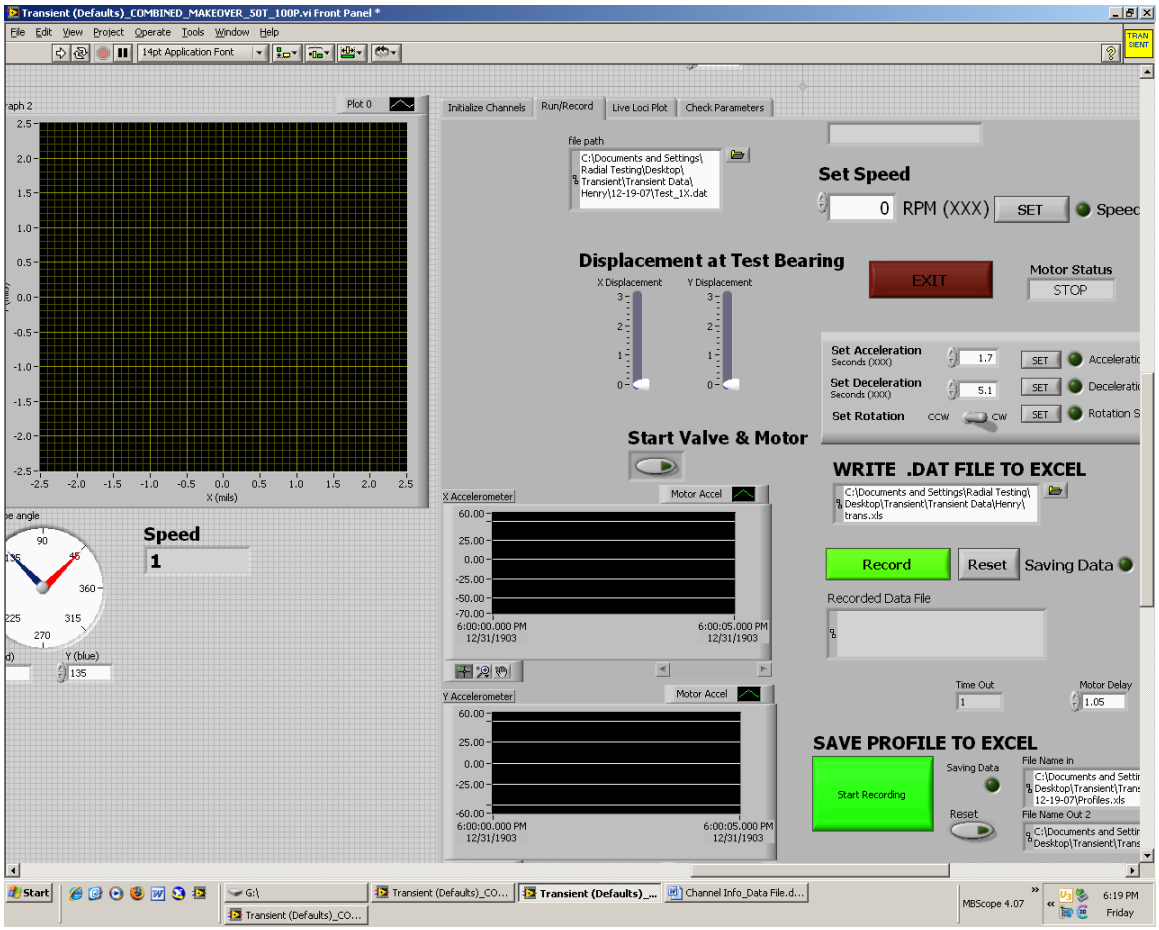

Fig. 43. Transient.vi Labview interface.

The back panel in the Transient.vi has the block diagram programming language. Software from the motor controller and the order analysis tool kit from Texas Instruments was used to develop the program to record the data during testing. Fig. 44 shows specific

examples from the program. The block diagrams show a time delay that was used to slow the start transient due to sluggish water pressure build up from the piping design.

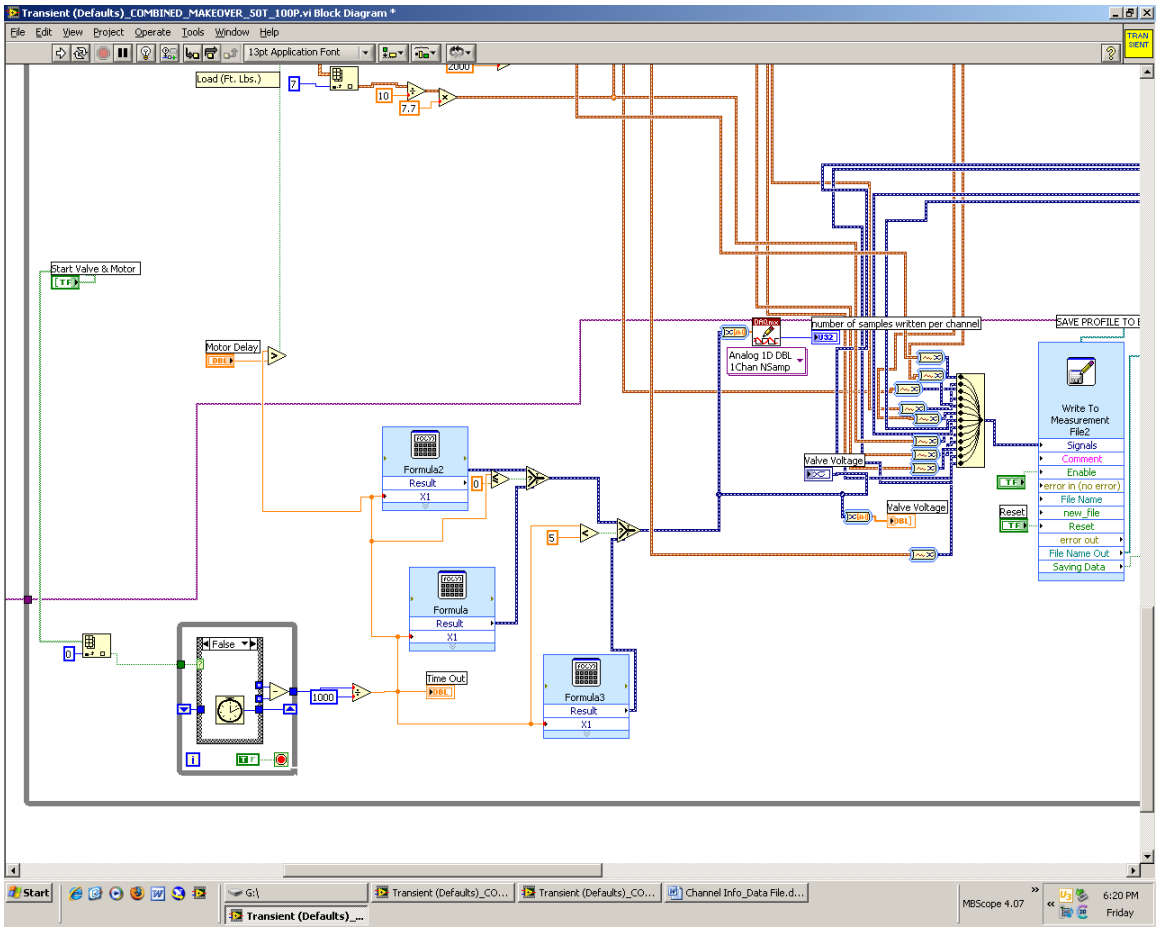

Fig. 44. Labview block diagram depicting the time delay and equation programming.

Fig. 45 shows parts of the program using tools from the order analysis tool kit used to initiate the channels for data recording. The tools allowed the program to tie specific characteristics to the data for each channel. For example, a tachometer signal can be separated from a prox probe signal due to the channel initialization. This allows for easier data manipulation.

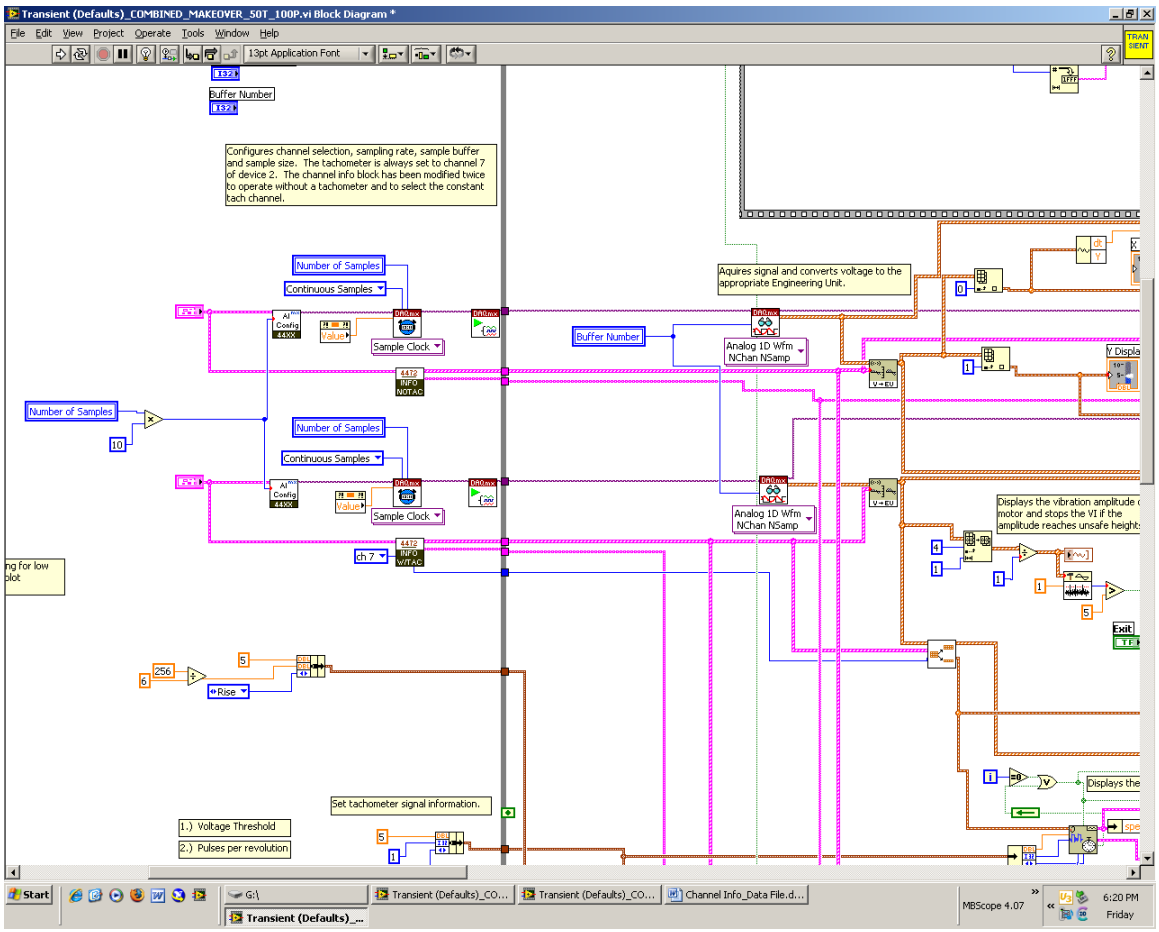

Fig. 45. Channel initialization software from Order Analysis Software from LabView.

Each channel of data was recorded into a .dat file and is considered raw unprocessed data. Specific channels were chosen for shaft centerline and lift-off speed analysis and was written into an excel spreadsheet. Fig. 46 shows the channels being routed to the excel writing software in the LabView program.

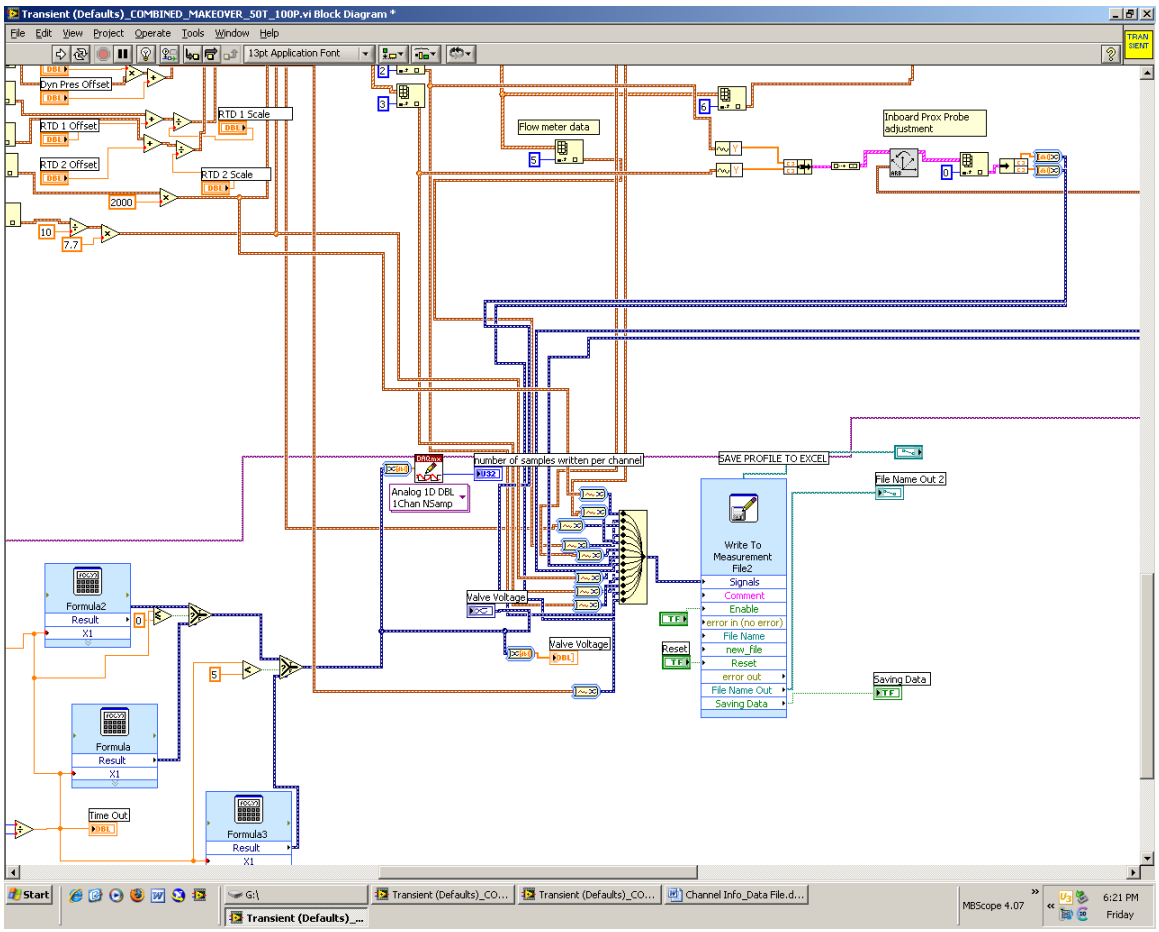

Fig. 46. Specific part of the block diagram that allows the info from the channels to be written in Excel.